

Chapter 5

3D field-data example

In this chapter, I apply ISWET using 3D-image-space generalized wavefields to estimate the migration-velocity model for the 3D North Sea dataset. The challenges for defining the velocity model for this dataset are due to a possibly irregular salt body, the intense faulting, the amplitude variations caused by irregular acquisition, the short source-receiver offsets, and the limited source-receiver azimuths. Because of the narrow azimuthal configuration, the 3D dataset was submitted to azimuth-moveout (AMO), and common-azimuth migration images are used as the initial conditions for the modeling of the 3D-image-space generalized datasets. This enables us to use very few image-space generalized wavefields in 3D-ISWET. For the velocity inversion we used a combination of layer-stripping ISWET and horizon-based tomography ISWET along with salt-flooding for defining the salt-body contours, yielding consistent velocity updates, fast convergence, and a geologically plausible velocity model. The excellent quality of the final image exposes the structural complexity by correctly imaging faults, satisfactorily unveiling the base of salt, and revealing sub-salt sediments.

INTRODUCTION

The 3D North Sea dataset spans over an area of approximately 55 km², with 13.5 km in-lines and 4 km cross-lines. It was acquired using dual sources at intervals of 25 m in the in-line direction and 50 m in the cross-line direction, with three cables with 100 m separation and a maximum offset 3600 m. The limited cross-line offsets (Figure 5.1d) resulting from this acquisition configuration impose limitations in the azimuthal distribution, as can be seen in Figure 5.1a and 5.1b. The overall in-line-offset distribution is quite regular (Figure 5.1c). However, the offset distribution is spatially quite irregular. The fold of coverage computed for a grid cell of 25 X 25 m for different offset ranges is shown in Figure 5.2. The acquisition footprint is evident, with a wide low-fold region occurring for in-lines around 4000 m in the y direction.

To mitigate the offset irregularity, considering the limited azimuthal distribution, Clapp (2005, 2006) applies least-squares 3D-data regularization using offset volumes transformed to a common offset via AMO (Biondi et al., 1998). In spite of the good imaging results, the amplitude variation caused by the offset irregularity, although diminished, still persists as can be seen in Figure 5.3. It shows time slices at 2.8 s through the trace envelope for different offset cubes taken from the regularized data provided by Clapp.

Even though the fold irregularity (Figure 5.2) and amplitude imbalance (Figure 5.3) are in the data-space, we will see later that they will be evident in the amplitudes of the gradient of the objective function at approximately the same spatial position.

The velocity model provided along with the data (Figure 5.4), herein called the original velocity model, presents a general layered structure with an overhanging salt dome connected to a deeper layer with the same velocity as that of the salt dome. In Figure 5.4, the maximum velocity is 4820 m/s. The final velocity model I derive shows remarkable differences when compared to the original velocity model, especially in the salt body shape.

I start ISWET with an initial velocity model derived from the original velocity model. Initially, the sediment velocity above the chalk layer was refined using residual

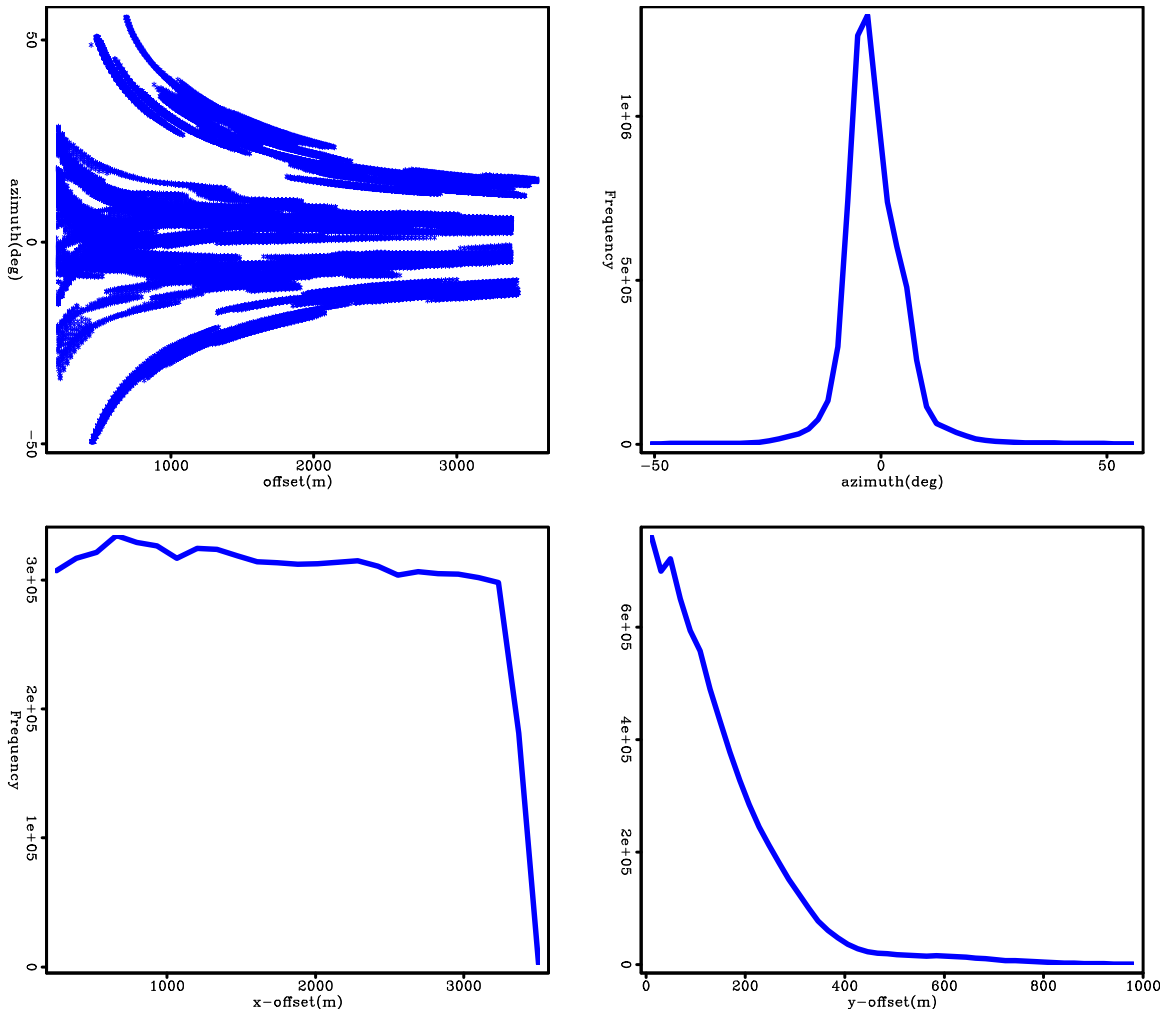


Figure 5.1: a) Offset – azimuth cross-plot, b) azimuth histogram, c) in-line offset histogram, and d) cross-line offset histogram. 3dex/. 3dex101

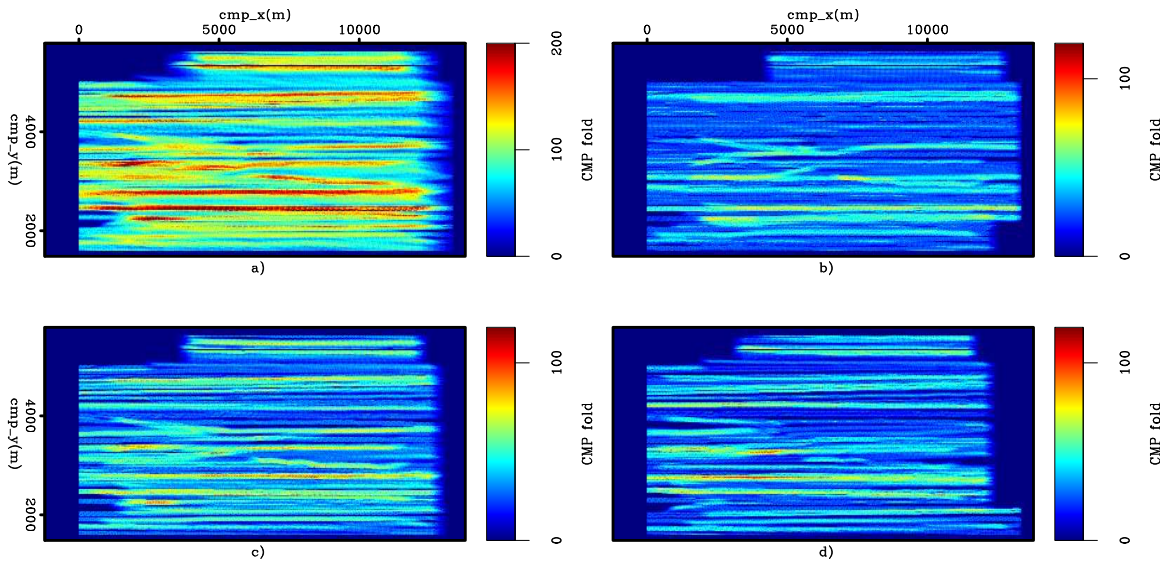


Figure 5.2: Fold of coverage plots: a) full offset, b) 0 – 1200 m offset, c) 1200 – 2400 m offset, and d) 2400 – 3600 m offset. 3dex/. 3dex102

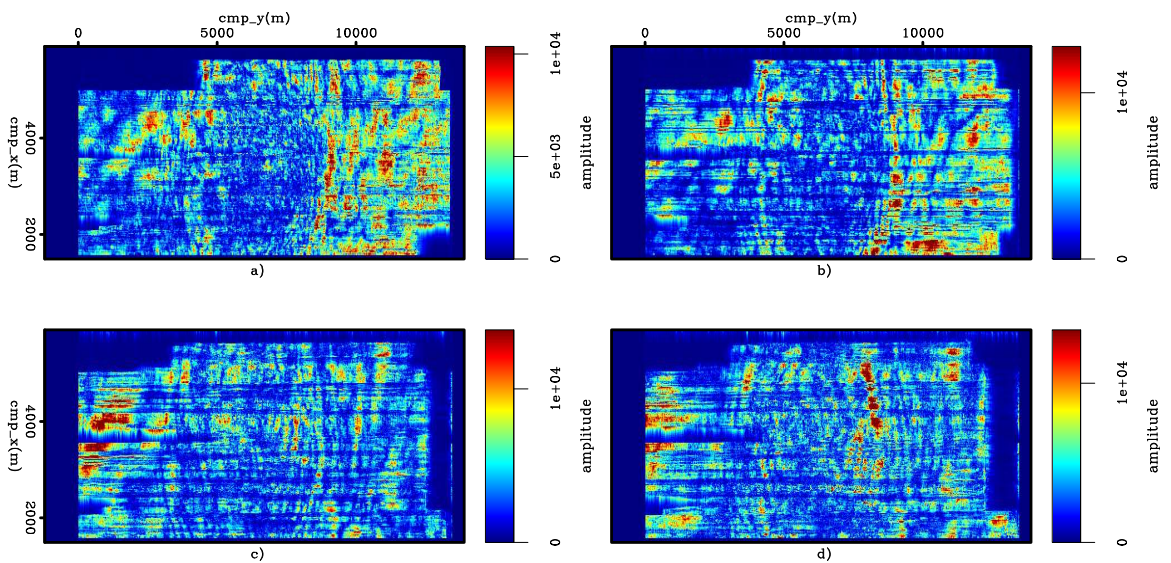


Figure 5.3: Time slices through the trace envelope for different offset cubes from the regularized data: a) offset 200m, b) offset 1200 m, c) offset 2400 m, and d) offset 3000 m. 3dex/. 3dex103

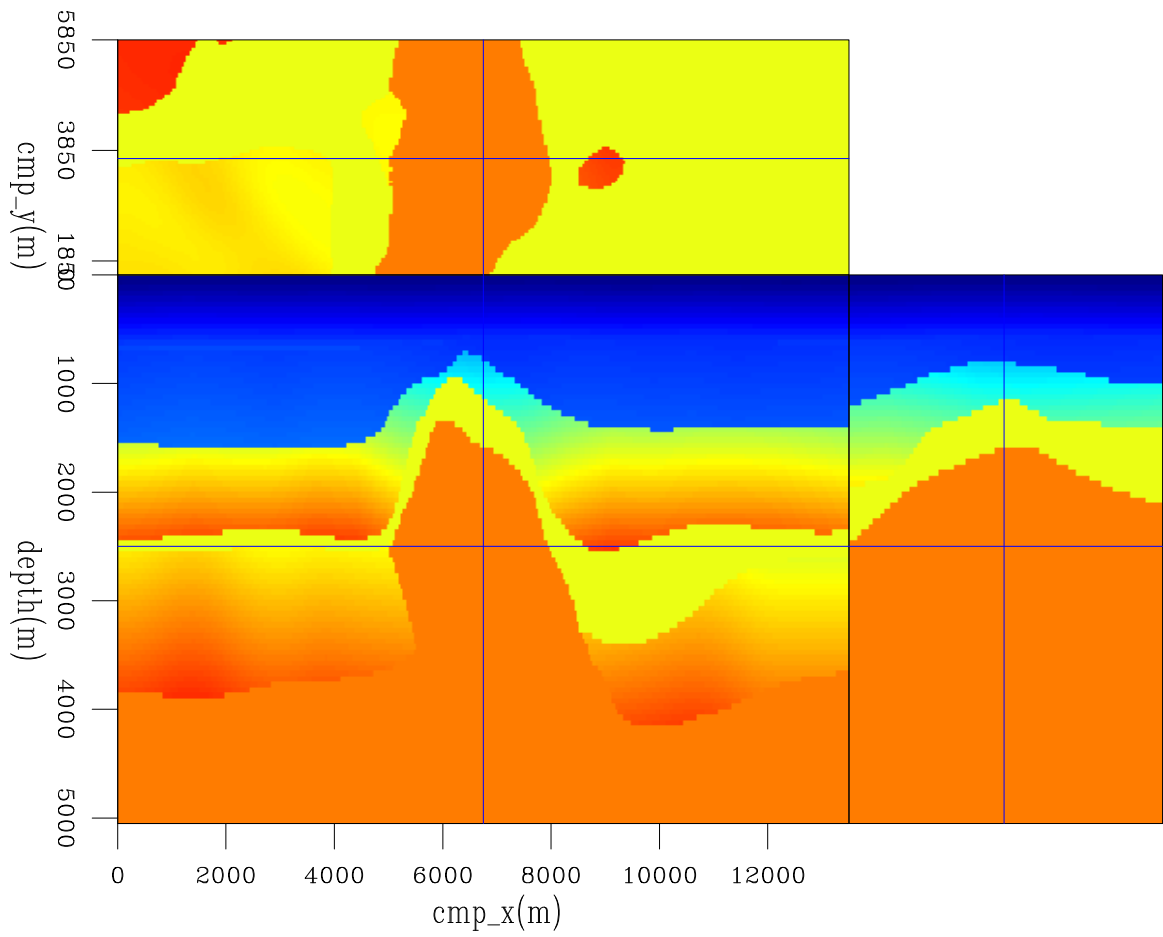


Figure 5.4: Slices through the IFP velocity model. 3dex/. 3dex104

prestack depth-migration scans. Then, I interpreted the top of chalk on an image migrated with this new velocity. Below the top of chalk, velocity was heavily smoothed using a 5000 m wide 2D median smoother. In addition, to increase the inaccuracy of the initial velocity model, velocity was scaled down by a factor of 0.9 (Figure 5.5). In Figure 5.5, the initial velocity model is displayed with the same color scale as that of Figure 5.4 and the maximum velocity is 4100 m/s. A layer-stripping approach was used to define the velocity for the chalk layer, considering a sufficiently accurate velocity for the sediments above. Then, the top salt was interpreted, and a salt flooding procedure enabled the interpretation of the base of salt. The interpretation of the base of salt can be considered the main source of uncertainty of the 3D-field data example, since no previous geological information was available. Finally, a group of reflectors below the salt is used to define the velocity structure for the deeper part.

All the computations were carried out on computer nodes of the Stanford Center for Computational Earth & Environmental Science (CEES). Thirty nodes of Dual Nehalem 5520 with 24Gb RAM were used, accounting to 240 CPUs. To generate 30 pairs of 3D ISPEWs, using 196 frequencies, it took 10 minutes. On average, each iteration of the velocity optimization, consisting of one function evaluation, the gradient computation, and two additional function evaluations for the line search, took approximately two hours.

In this chapter, I give details of the procedures above, which led to a final image with quality superior to that of the image computed with the initial velocity model, as well as to that obtained with the original velocity model. I show that using image-space generalized wavefields lends flexibility and computational efficiency to 3D-ISWET, while maintaining the necessary robustness.

IMPROVING VELOCITY ABOVE THE CHALK

When defining the depth-migration velocity model, it is very important that velocity in the shallow layers is sufficiently accurate, so that velocity errors are not propagated to deeper layers. A first version of the initial velocity Figure 5.6 was generated in

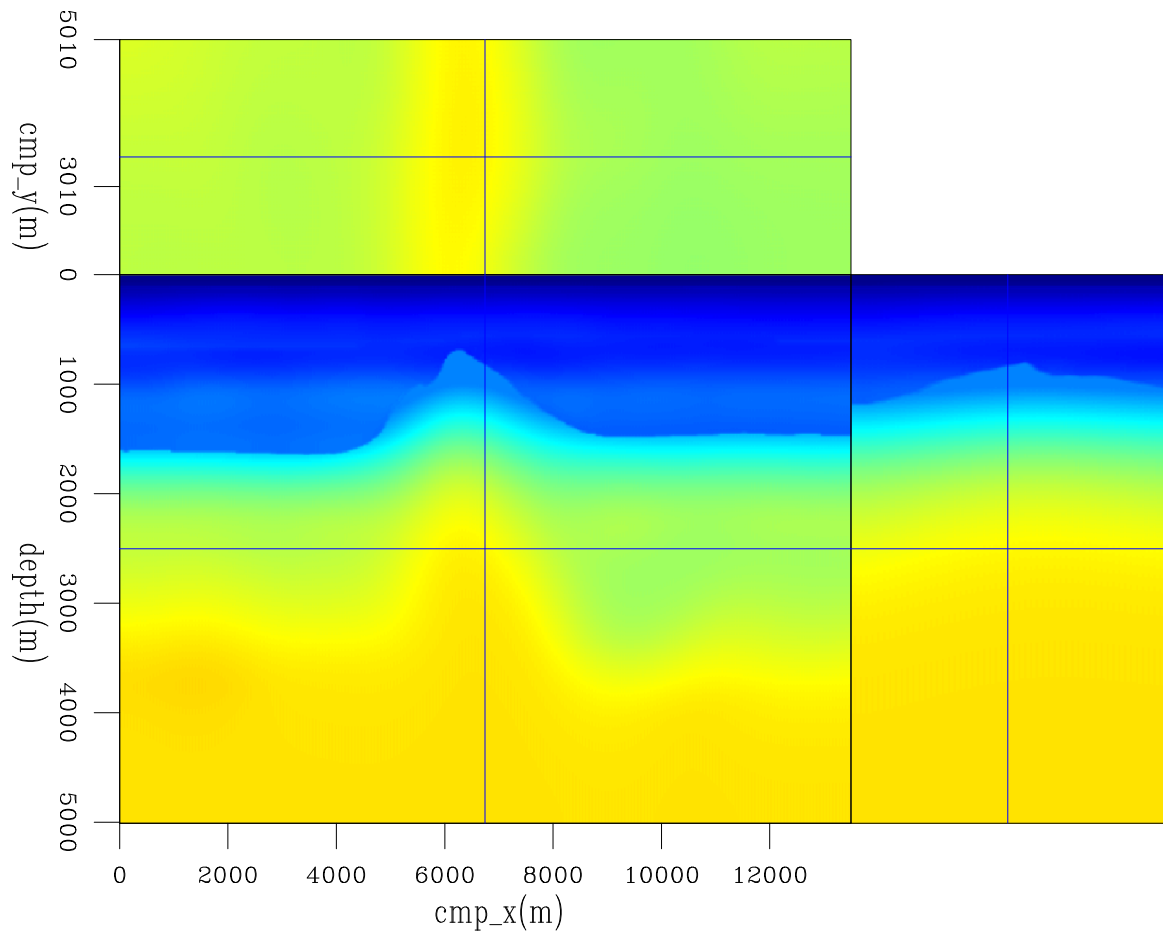


Figure 5.5: Slices through the initial velocity model used in 3D-ISWET.
3dex/. 3dex105

a similar way as that for Figure 5.5, except that the velocity above the top of the chalk is the same as the original velocity. Migration with this version of the initial velocity revealed slight velocity inaccuracies for the sediment layer above the chalk, evidenced by residual moveout in the SODCIGs (Figure 5.7). The section on the top is the zero-subsurface-offset section, and the panels at the bottom are SODCIGs at the position corresponding to their x coordinates. Notice the shallow events curving down in the SODCIGs, especially for x coordinates below 6000 m. The strong reflector, which is flat at depths of 1500 m on the left and 1300 m on the right, and curved in the middle of the figure, is the top of chalk. It also presents strong curvature. The residual moveout of these gathers was evaluated with residual-prestack-depth migration velocity analysis (Sava, 2003), in which a residual moveout parameter was interpreted. Since the velocity structure is approximately one-dimensional and the residual-moveout parameter is local, I performed one run of a simple vertical velocity update similar to Deregowski's velocity update (Deregowski, 1990).

The new velocity model satisfactorily improved the focusing of the image, as can be seen in Figure 5.8. Notice how both the shallow reflectors and the top of chalk are much better focused around zero-subsurface offset. Also, since the interval velocities increased, the top of chalk is shifted down. The maximum frequency used to compute images of Figures 5.7 and 5.8 is 60 Hz. For velocity optimization and the following common-azimuth migration images, the maximum frequency is 42 Hz.

SOLVING FOR THE CHALK LAYER VELOCITY

Generating 3D ISPEWs for the base of chalk

After improving the accuracy of the initial velocity model for the shallower sediment layers, as previously discussed, common-azimuth migration (CAM) with this initial velocity (Figure 5.5) produced the images in Figure 5.9, which shows the volume for the zero subsurface offset, and Figure 5.10, which shows the zero subsurface offset on the left, and ADCIGs on the right for in-line 3180. The effects of migrating with a

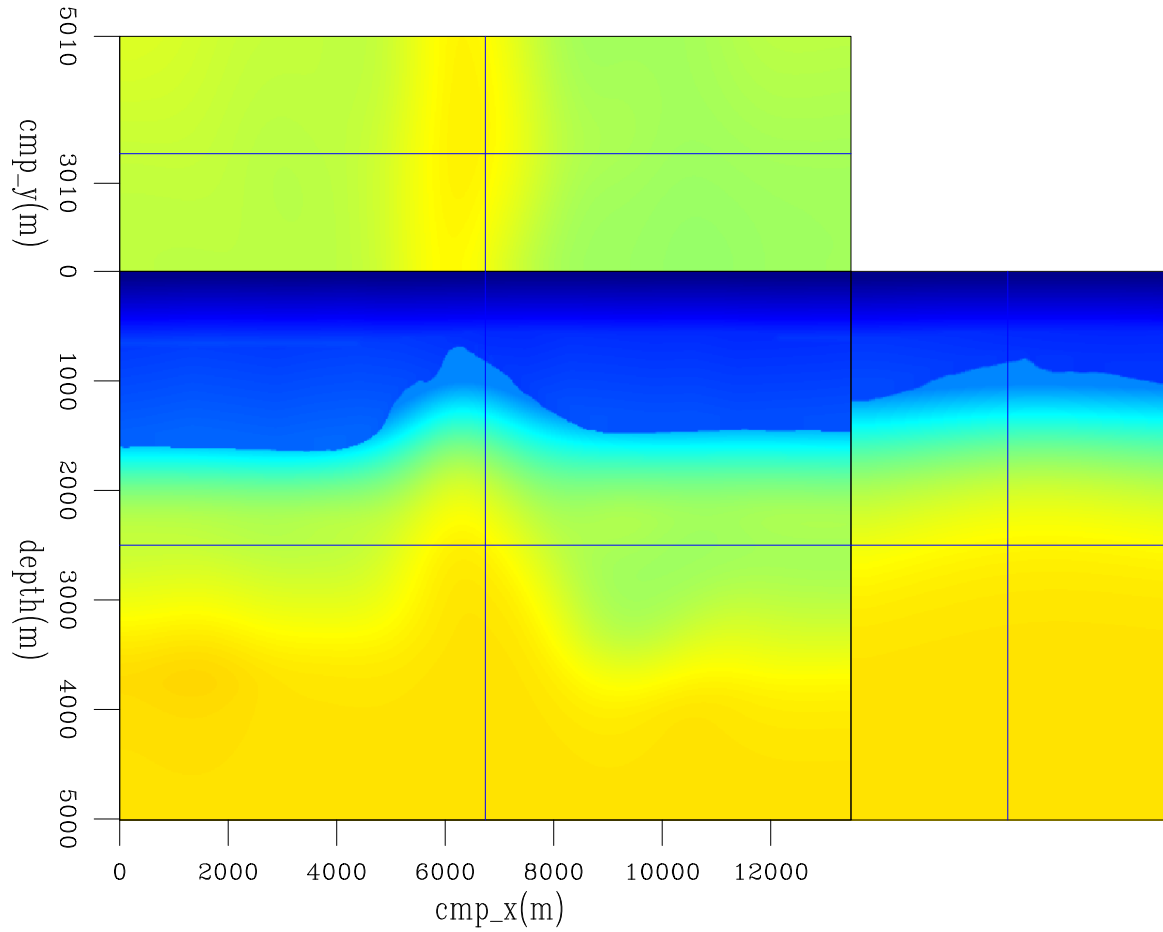


Figure 5.6: Slices through an initial velocity model generated with the same procedures as that for Figure 5.5, except for the velocity above the chalk, which is the original velocity. `3dex/. 3dex1051`

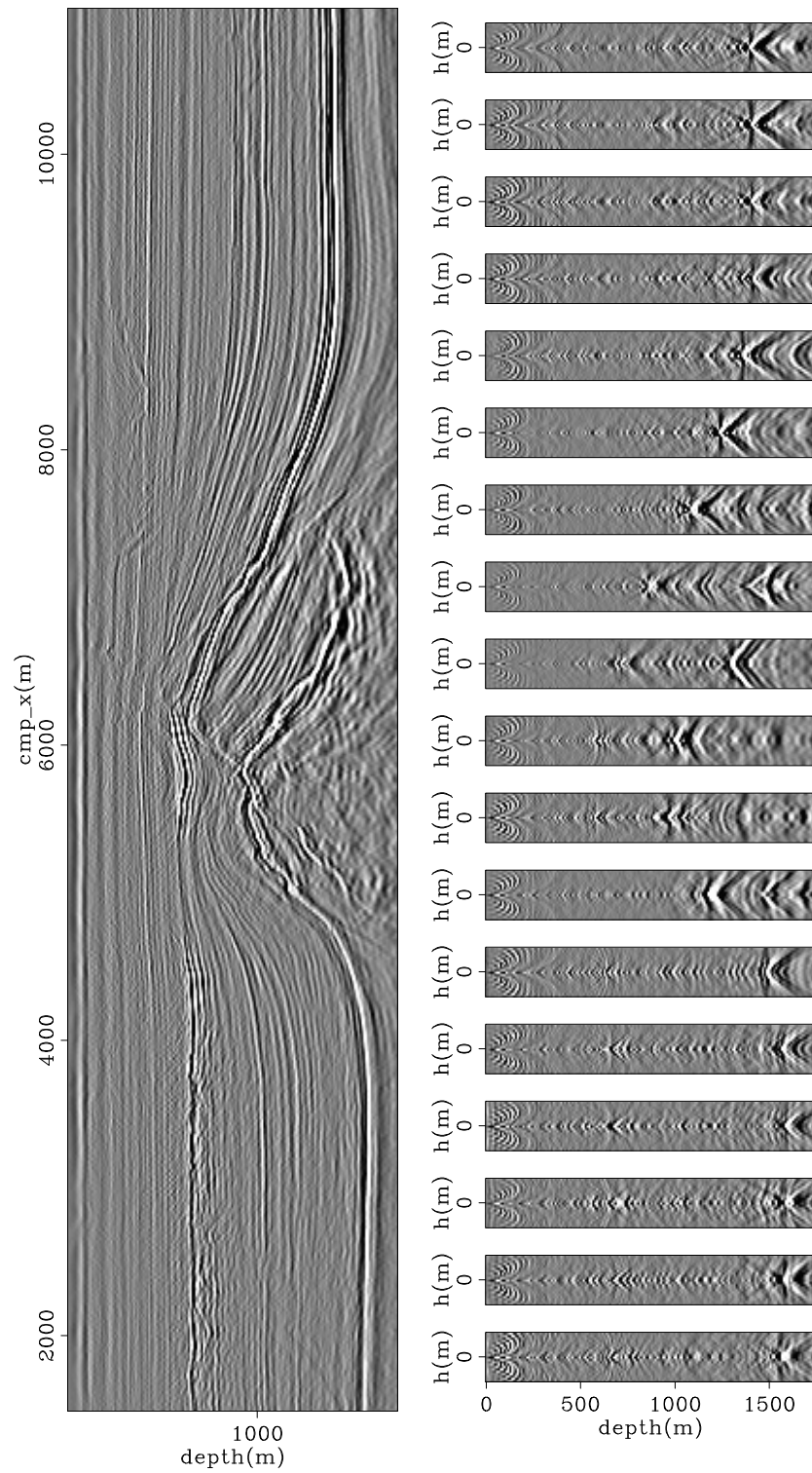


Figure 5.7: Image computed with the velocity model of Figure 5.6. The top panel is the zero-subsurface offset section and the panel at the bottom are the SODCIGs.

3dex/. 3dex100

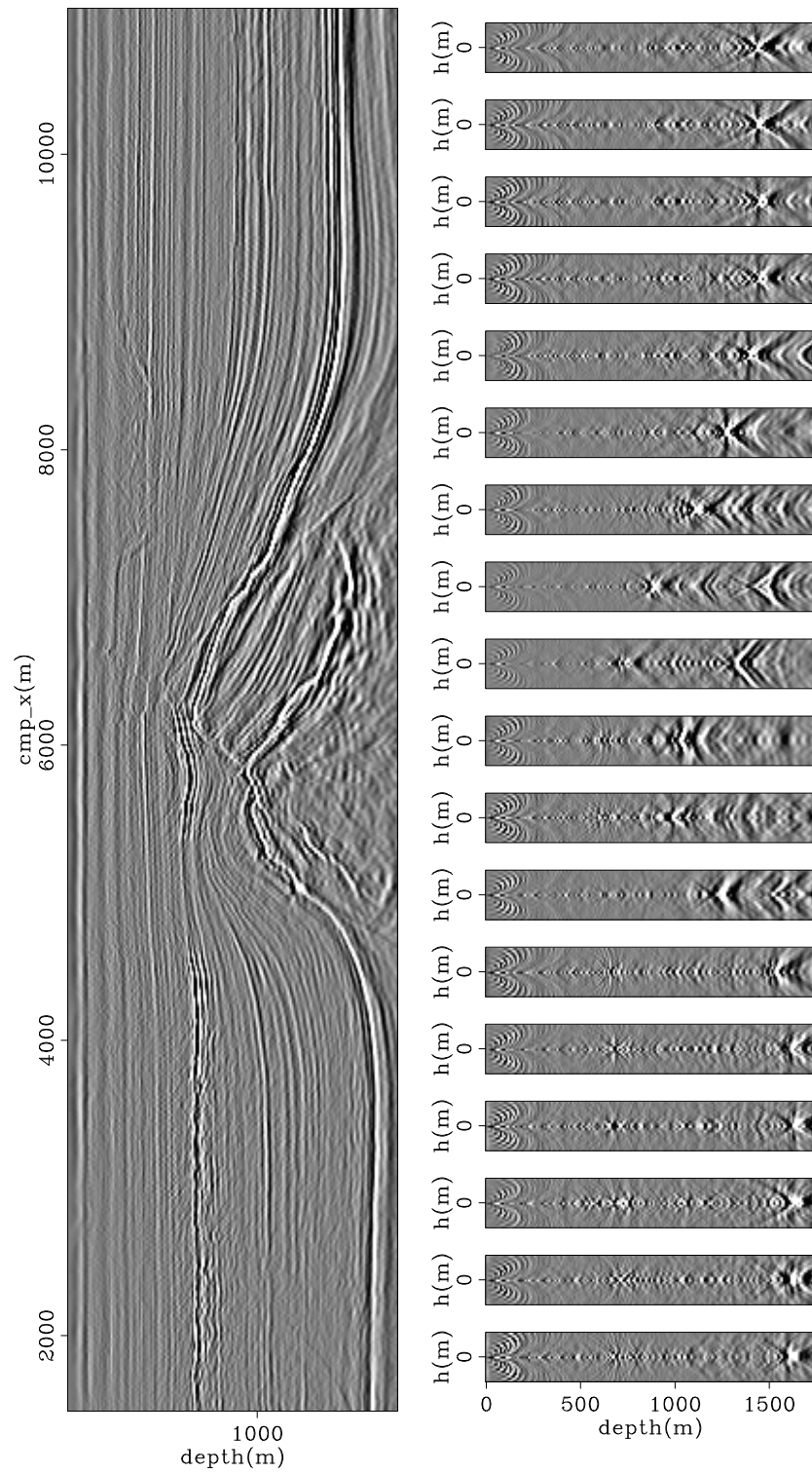


Figure 5.8: Image computed with the velocity model of Figure 5.5. The left panel is the zero-subsurface offset section and the panels on the right are the SODCIGs. Compare with Figure 5.7. 3dex/. 3dex1000

too low velocity are evidenced by poorly collapsed diffractions close to the salt flank, poorly imaged faults, and reflectors curving up in the ADCIGs.

For the modeling of ISPEWs, in-line and cross-line intervals of the CAM image were interpolated from 20 m to 30 m, which are the in-line and cross-line intervals used for optimizing the migration velocity. The base of chalk was interpreted in the 3D pre-stack volume, using the latest version of the hypercube viewer (Clapp et al., 2008).

After migration, the wavelet is velocity- and dip-dependent (Tygel et al., 1994). Although simple in 2D, implementing 3D windowing based on the dip- and velocity-dependent wavelet stretching can be cumbersome. Instead, I use a simpler procedure that yields a mask operator to window the reflector. First, I use the pre-stack interpretation to vertically window the target reflectors. Then, for each windowed subsurface-offset cube, I compute the tridimensional envelope with the same smoothing parameter in all directions, which simulates the dip dependency. The amplitudes are clipped to one, based on a threshold value. Amplitude variations are compensated for by applying an RMS gain prior to the computation of the envelope. The mask operator is shown in Figure 5.11 for the zero subsurface offset (Figure 5.11a) and for the in-line 3520 (Figure 5.11b), in which a subsurface-offset gather is shown on the right.

We extract the signed square root of the windowed pre-stack image to minimize the influence of the squaring of the wavelet on the gradient computation, as discussed in Chapter 4.

As shown in Chapter 2, the CAM initial conditions can be continuously sampled in the cross-line direction, because no cross-line offset is computed; this reduces by at least one order of magnitude the number of image-space generalized wavefields to be synthesized. For the base of chalk, we modeled only 30 3D ISPEWs, which are collected at 600 m depth. Using 30 CEES nodes with 8 CPUs each, the modeling takes approximately 10 minutes. A pair of 3D-ISPEW gathers is shown in Figure 5.12. Since the number of subsurface offsets that will be used during ISWET is 25

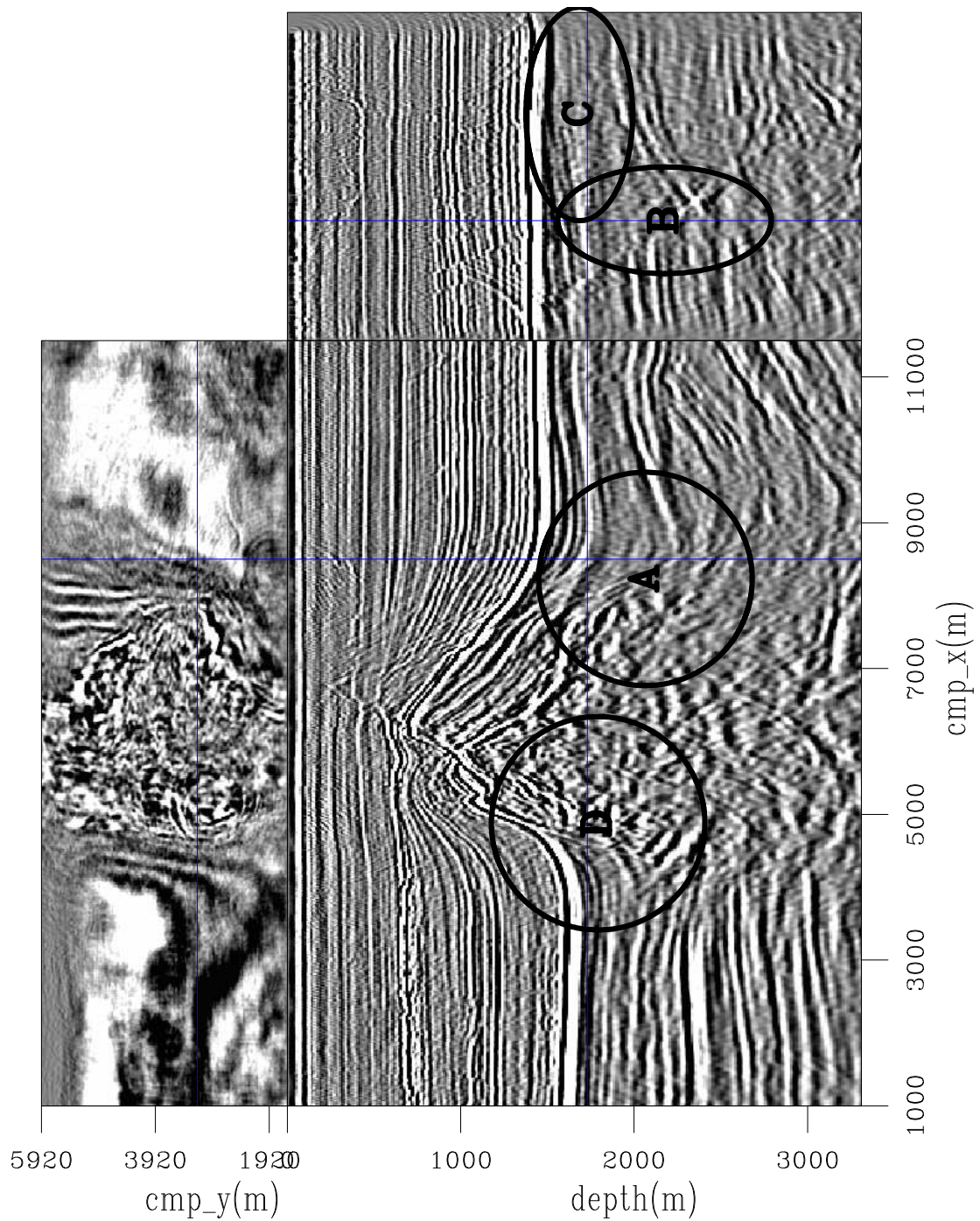


Figure 5.9: Slices through the CAM image with the initial velocity model of Figure 5.5. Notice poorly collapsed diffractions close to the salt flank (A and D), and poorly imaged faults (B and C) caused by migrating with an inaccurate velocity.

3dex/. 3dex106

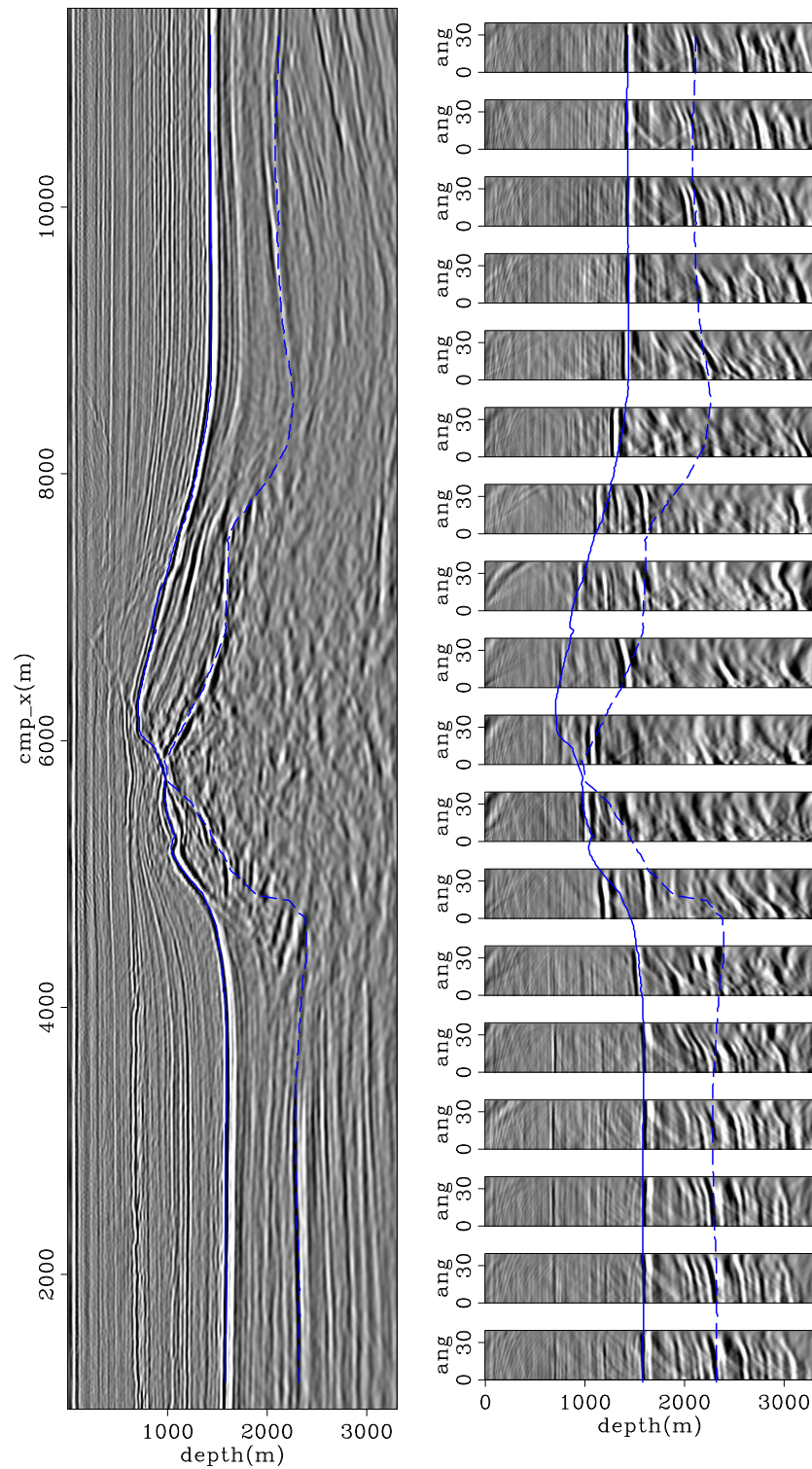


Figure 5.10: In-line 3180 of the CAM image with the initial velocity model of Figure 5.5. On the left is the zero-subsurface offset section, and on the right ADCIGs. Notice the strong residual moveout on the ADCIGs. The continuous blue line is the top of chalk, and the dashed blue line it the base of chalk. `3dex/. 3dex1073180`

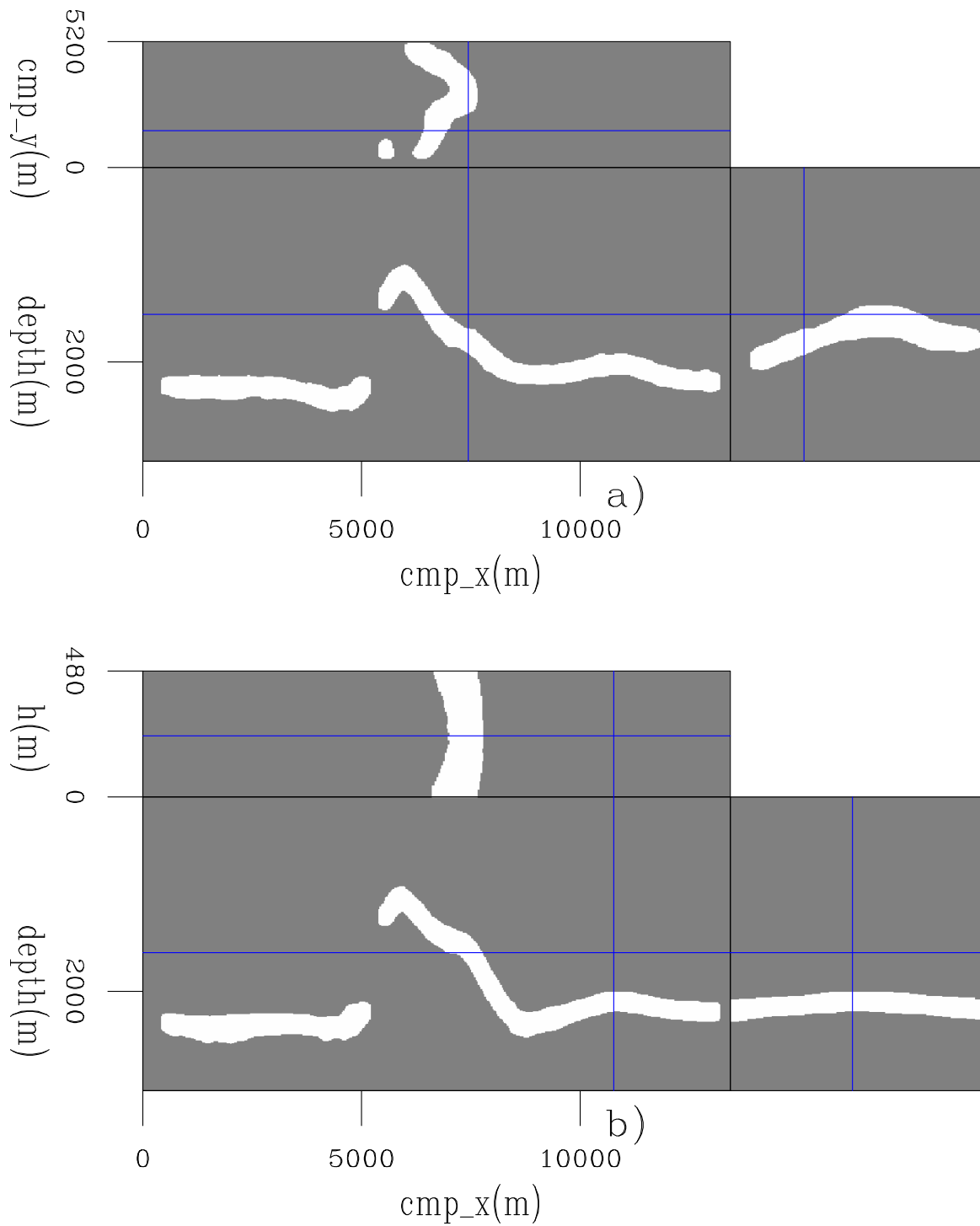


Figure 5.11: Slices through the prestack-mask operator to select the base of chalk, showing: a) the zero subsurface offset, and b) the in-line 3520. 3dex/. 3dex106a

and the spatial sampling in the x direction of 30 SODCIGs is used to model the 3D ISPEWs, crosstalk is expected to be strongly attenuated during imaging in ISWET.

Velocity optimization

A nonlinear conjugate-gradient solver is used for the velocity optimization. Velocity update is constrained to a maximum of 10% variation between iterations. All the wavefield propagation is performed between the depth at which the 30 3D ISPEWs were collected (600 m) and the maximum depth (3300 m). Velocity is updated up to the top of the chalk layer.

The amplitude variations are more pronounced in 3D than in 2D because of the acquisition footprint. To illustrate the amplitude variation problem, we compute the slowness perturbation without applying smoothing, and without extracting the signed square root from the initial conditions, to model 30 pairs of ISPEWs (Figure 5.13). In this case, the amplitude variation due to acquisition is even more pronounced. The acquisition footprint is clear, specially around the y coordinate 4000 m, which is a region with low-fold of coverage (Figure 5.2). If we extract the signed square root of the initial conditions for the modeling, or equivalently the signed fourth root of the gradient, the DSO slowness perturbation presents smaller amplitude variations (Figure 5.14).

The gradient of the objective function must be smooth to yield velocity updates consistent with the Born approximation, as discussed in Chapter 4. We apply a B-spline smoothing with node intervals of 420 X 420 X 160 m in the in-line, cross-line and depth directions, respectively. Applying B-spline smoothing on the DSO slowness perturbation of Figure 5.14 mitigates the amplitude-variation problems and yields consistent slowness perturbations (Figure 5.15).

Two runs of ISWET were necessary to define the velocity model for the chalk layer. In the first, we used the 30 pairs of ISPEWs whose modeling was described in the previous subsection. We used two function evaluations in the line search. After seven iterations, optimization stopped because the variation of the objective function

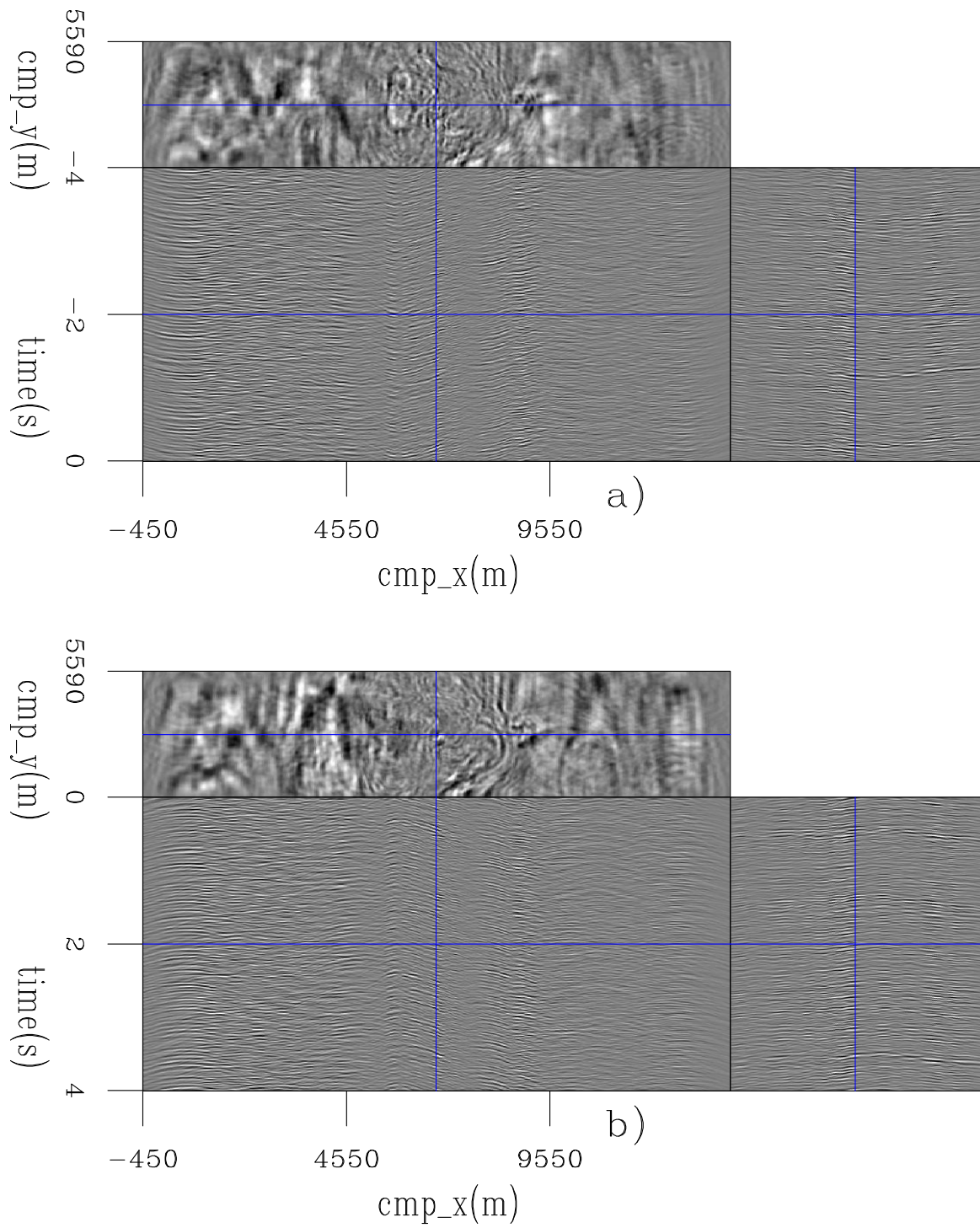


Figure 5.12: A pair of 3D source (a) and receiver (b) ISPEWs computed for the base of chalk. 3dex/. 3dex109

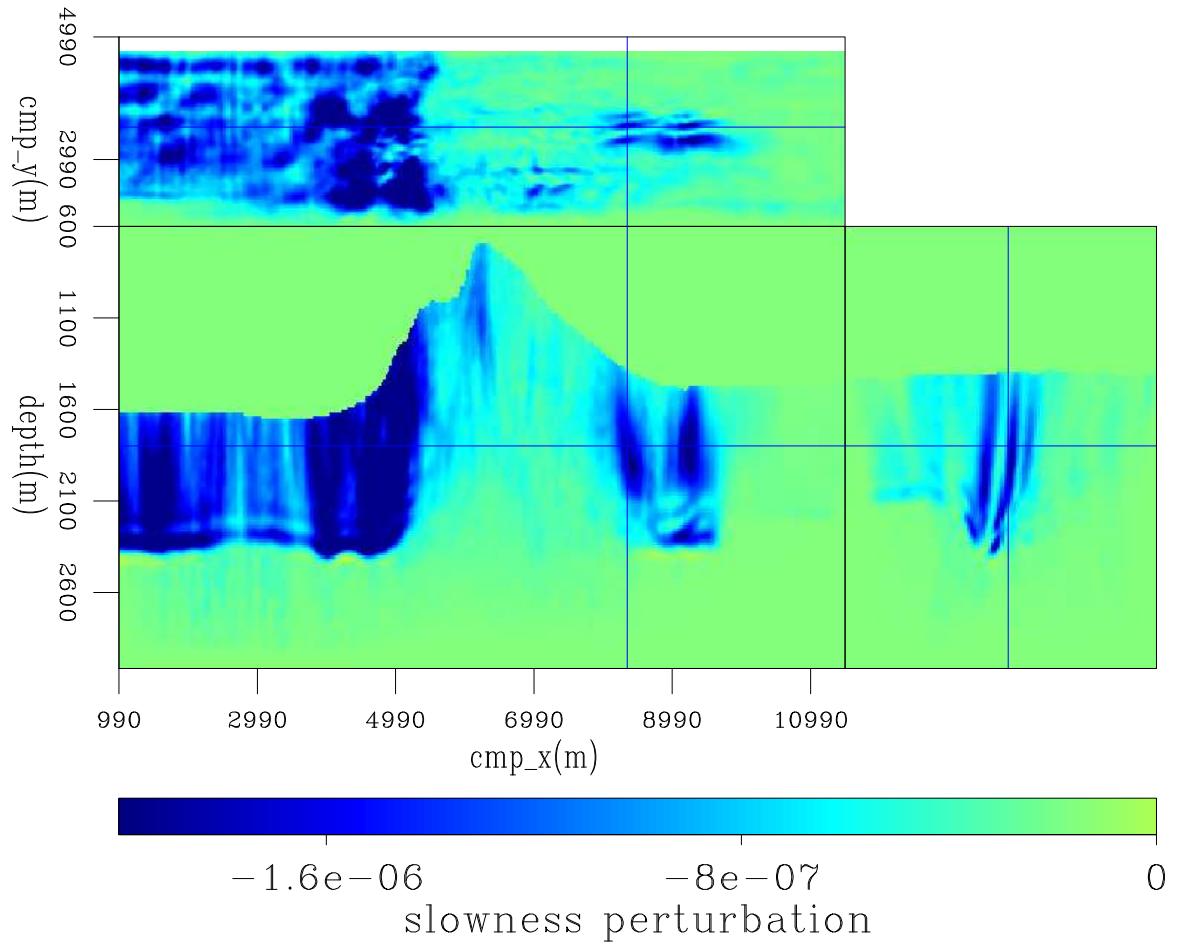


Figure 5.13: Slowness perturbation without smoothing and without extracting the signed square root from the initial conditions for the modeling of 30 pairs of ISPEWs. `3dex/. 3dex210`

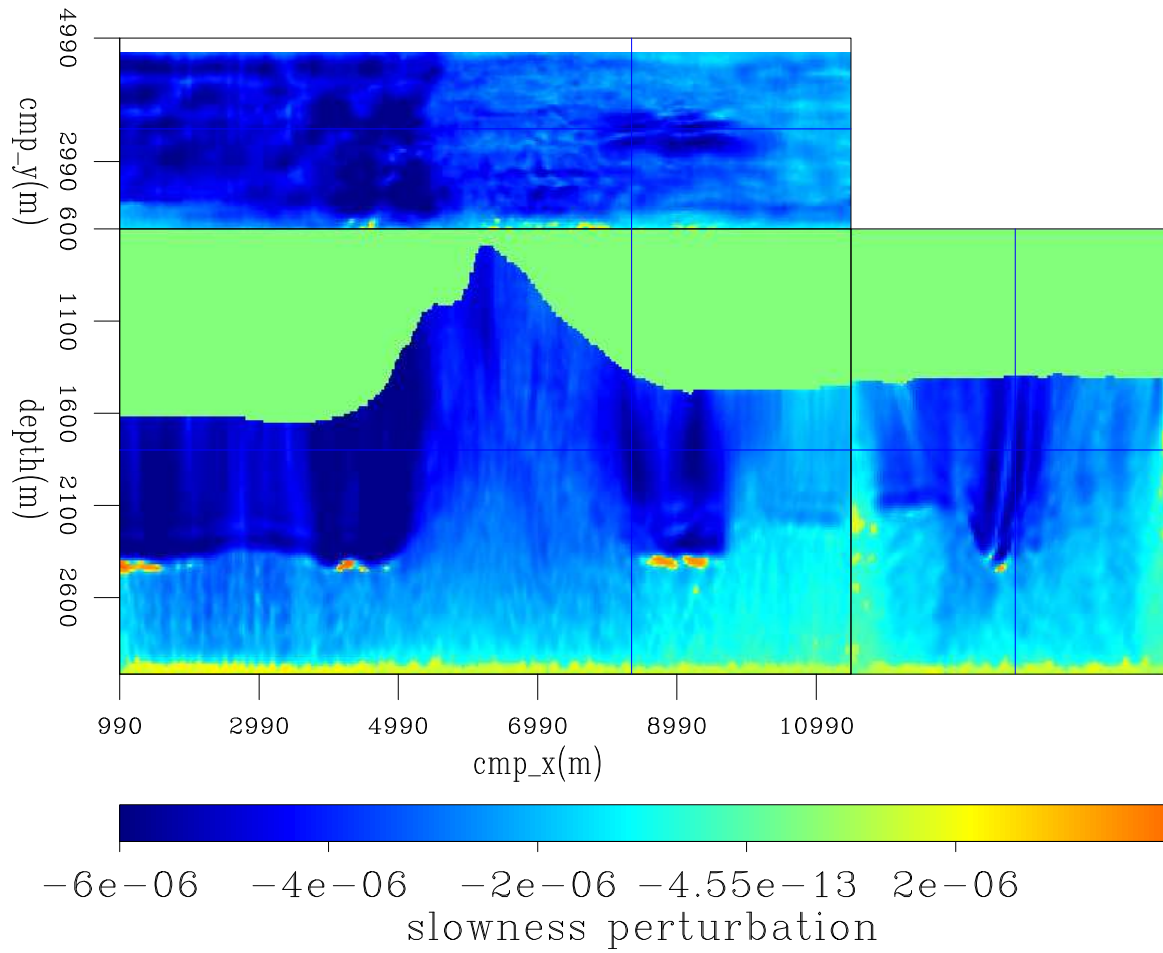


Figure 5.14: Slowness perturbation without smoothing and extracting the signed fourth root of the gradient. `3dex/. 3dex211`

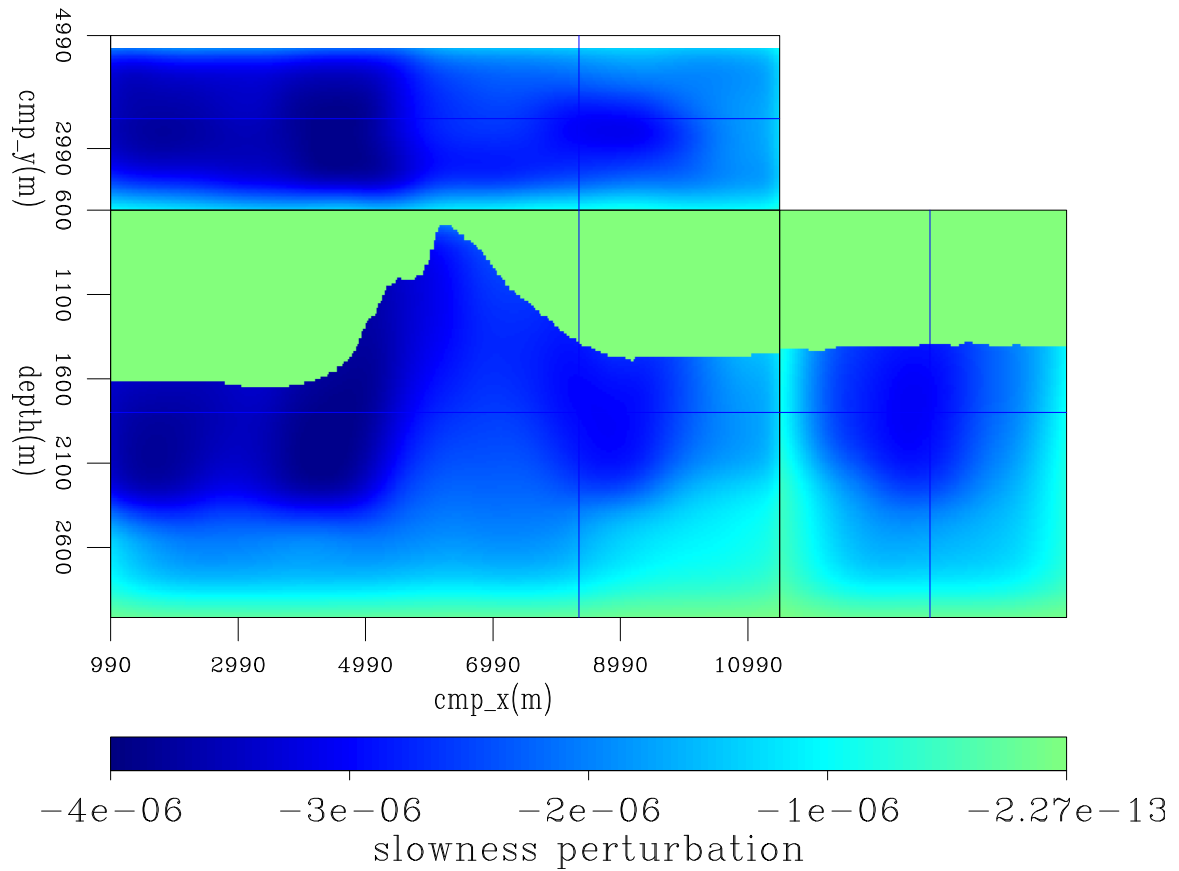


Figure 5.15: Slowness perturbation after B-spline smoothing the slowness perturbation of Figure 5.14. `3dex/. 3dex212`

was smaller than 0.1%. Figure 5.16 shows the evolution of the objective function.

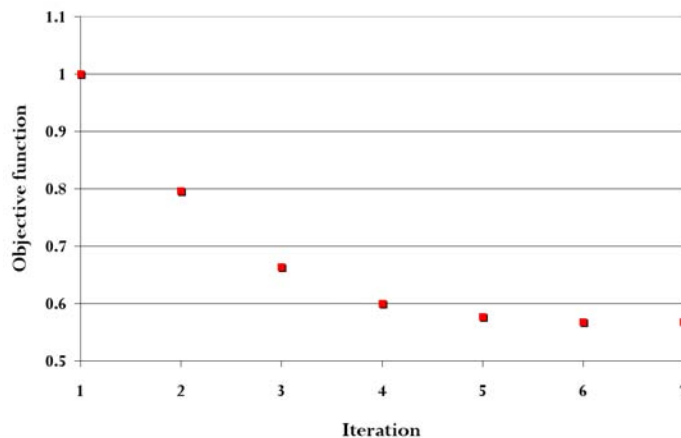


Figure 5.16: Evolution of the DVSA objective function for the first run of ISWET for the base of chalk. `3dex/. 3dex213`

The optimized velocity for the first run of ISWET is shown in Figure 5.19. As expected, the migration velocity increased compared to the initial velocity of Figure 5.5. The initial background image and the background image of the seventh iteration can be seen in Figures 5.17 and 5.18, respectively. On the left is the zero-subsurface-offset section, and on the right are the SODCIGs. Overall, the focusing around the zero subsurface offset improved. However, close to the salt flanks, SODCIGs still show events curving down, indicating velocity inaccuracy.

The velocity inaccuracy close to the salt flanks motivated a second run of ISWET for the base of chalk. Again, 30 pairs of ISPEWs were modeled, but from initial images limited to approximately 2 km around the salt body. By doing this, we explore the localized nature of these wavefields, as discussed in Chapter 2, so that this second run is targeted for updating the velocity close to the salt flanks. The optimized velocity for the second run of ISWET is shown in Figure 5.20. Migration velocity further increased compared to the optimized velocity of the first run (Figure 5.19). CAM using this optimized velocity is shown in Figure 5.21, which shows the volume for the zero subsurface offset, and Figure 5.22, which shows the zero subsurface offset on the top, and ADCIGs at the bottom for in-line 3180. Compare these figures with Figures 5.9 and 5.10, respectively. The optimized velocity model allowed imaging of a complex fault system on the right of the salt body, collapsing diffractions from the

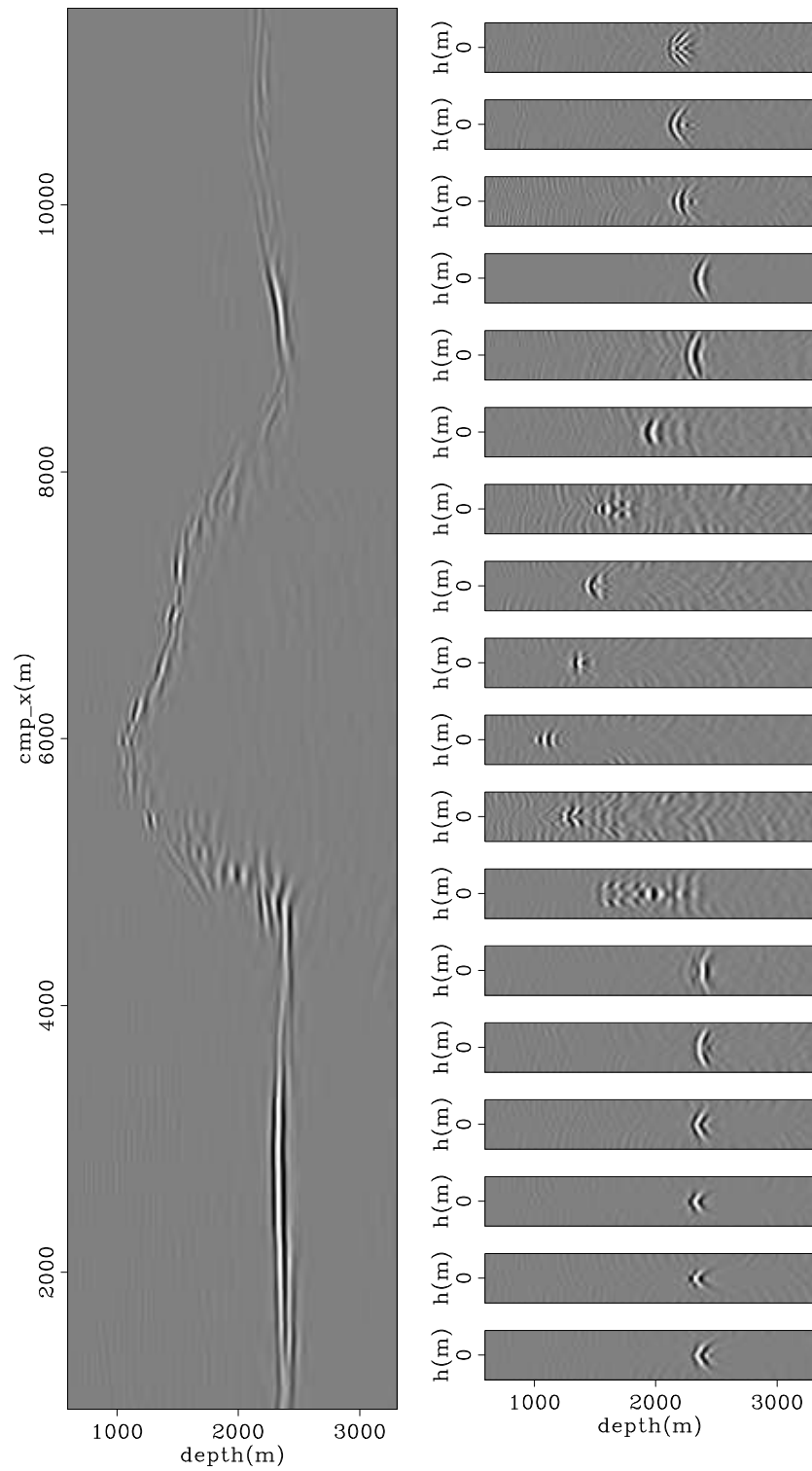


Figure 5.17: In-line 3520 of the initial background image of the first run of ISWET for the base of chalk. 3dex/. 3dex214

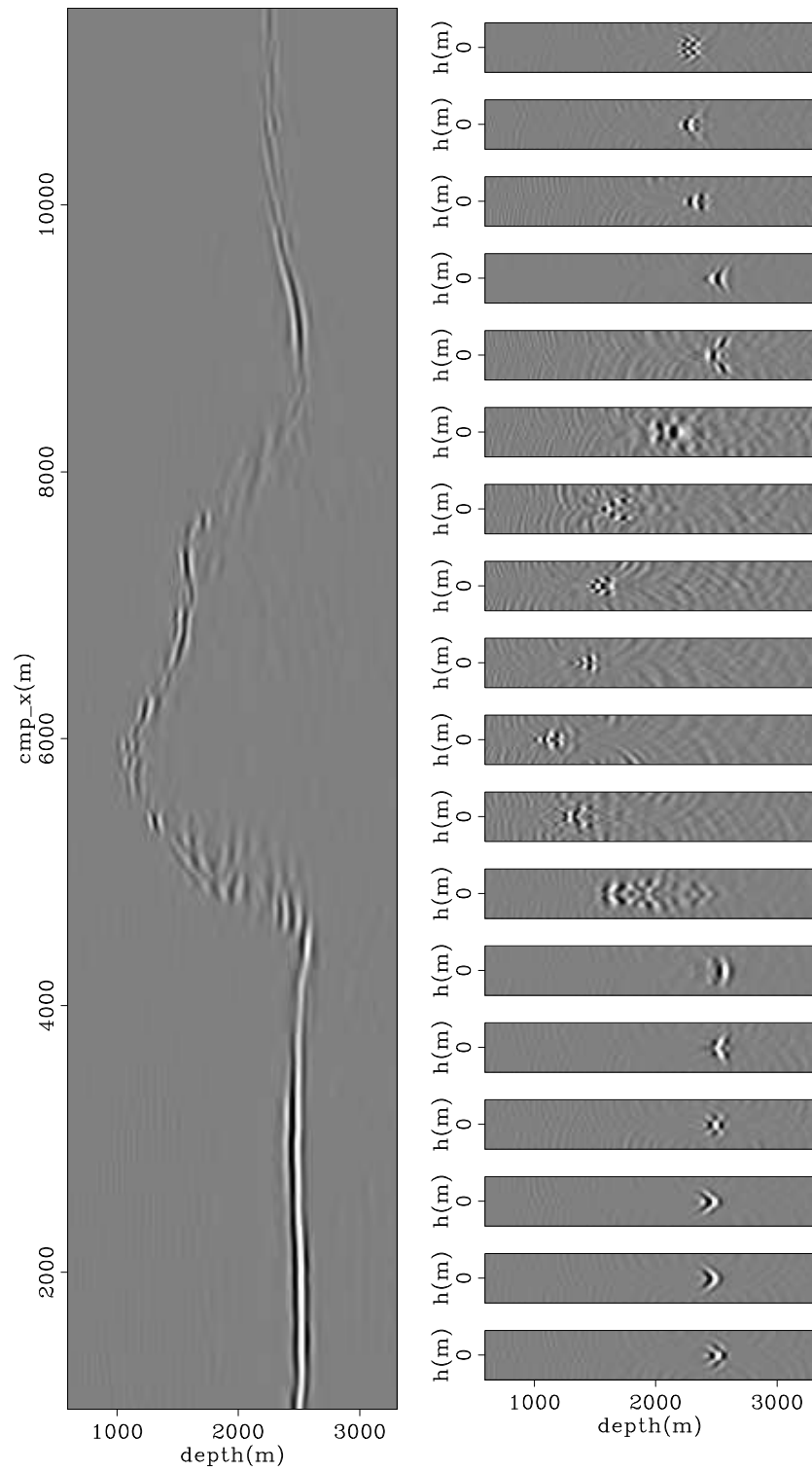


Figure 5.18: In-line 3520 of the background image computed with the optimized velocity model of the first run of ISWET for the base of chalk. 3dex/. 3dex215

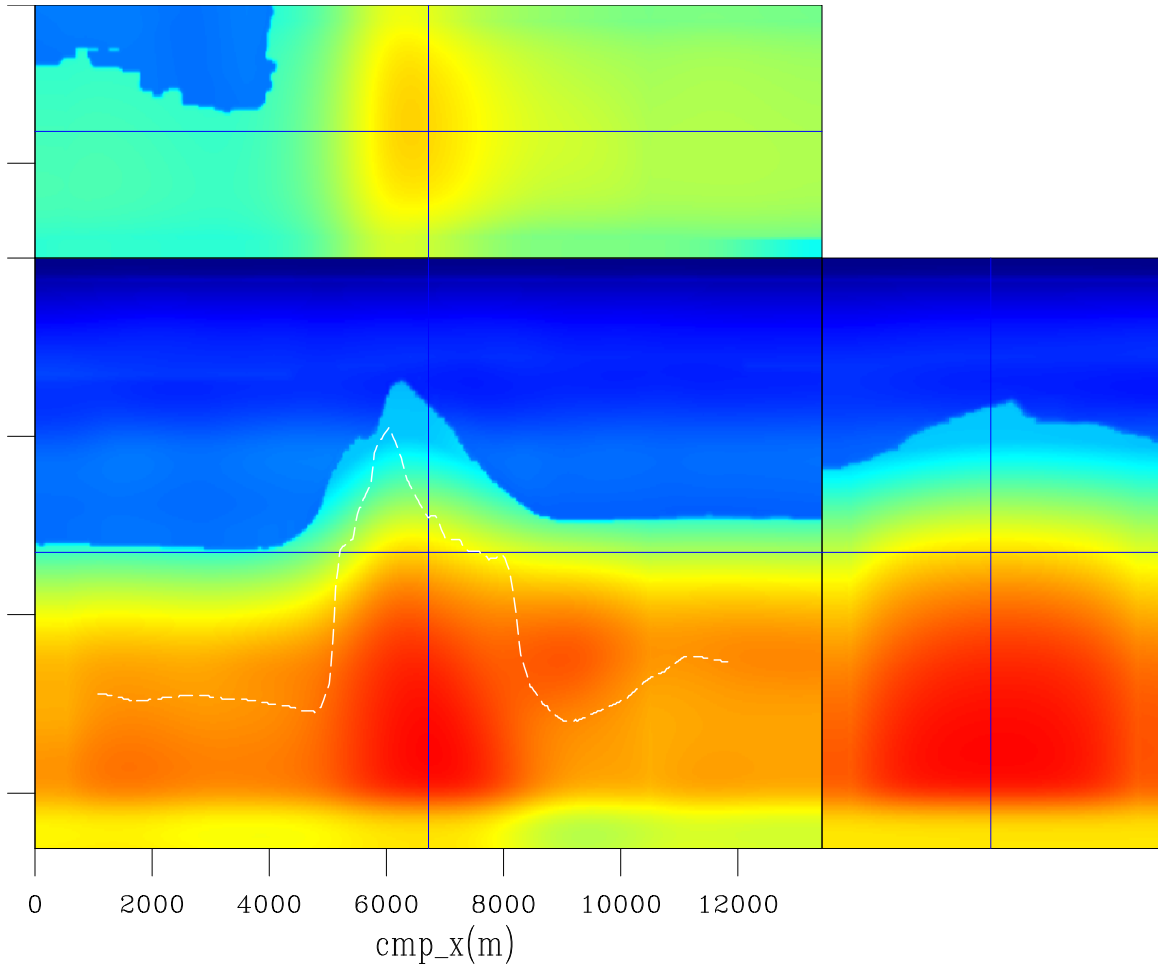


Figure 5.19: Slices through the optimized velocity from the first run of ISWET for the base of chalk. The dashed white line approximately represents the base of chalk.

3dex/. 3dex216

salt flank, and flattening reflectors in the ADCIGs.

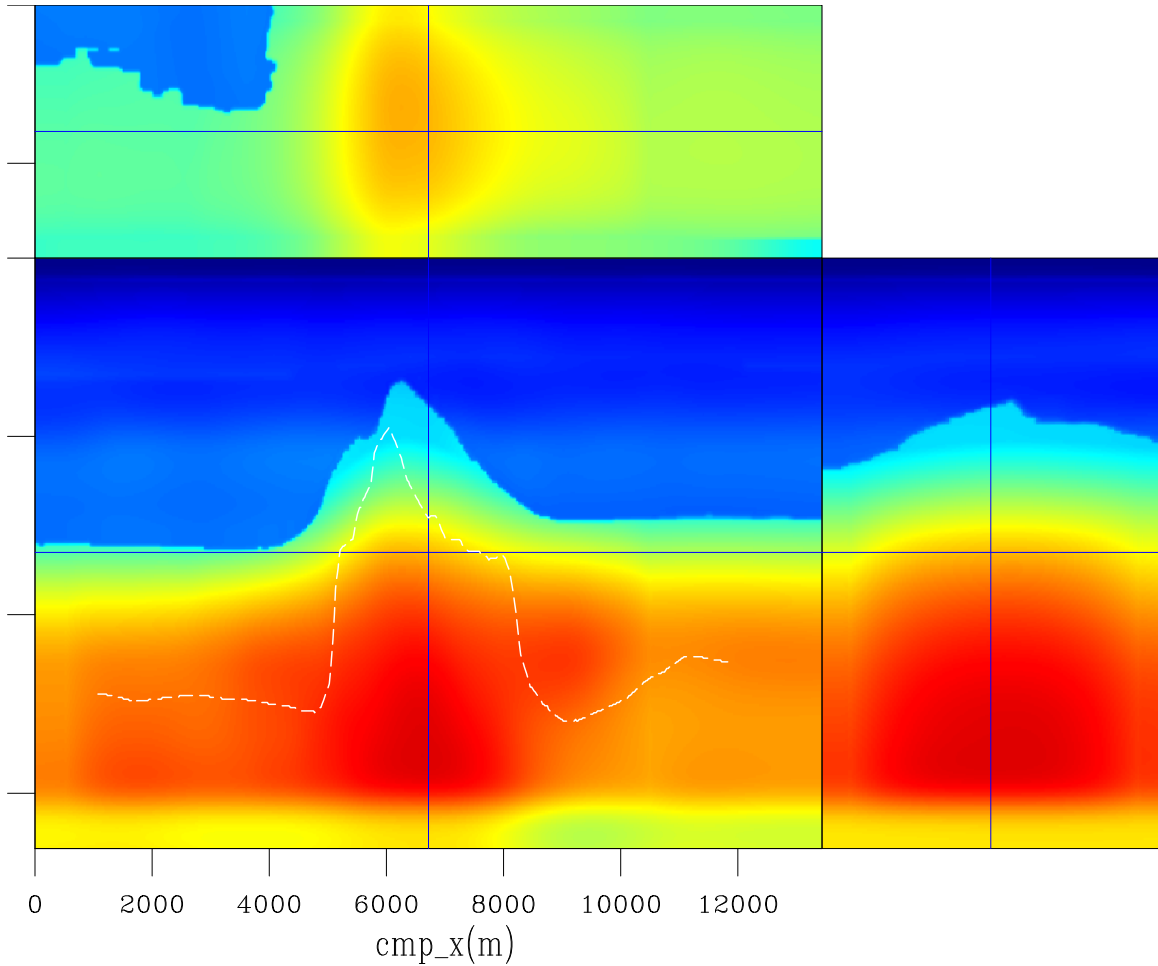


Figure 5.20: Slices through the optimized velocity from the second run of ISWET for the base of chalk. The dashed white line approximately represents the base of chalk.

3dex/. 3dex217

SALT FLOODING

Once a sufficiently accurate velocity for the chalk layer had been defined, salt flooding was used to delineate the salt body. The top salt was interpreted, and below the velocity was replaced by a constant value of 4500 m/s (Figure 5.23). The picking of

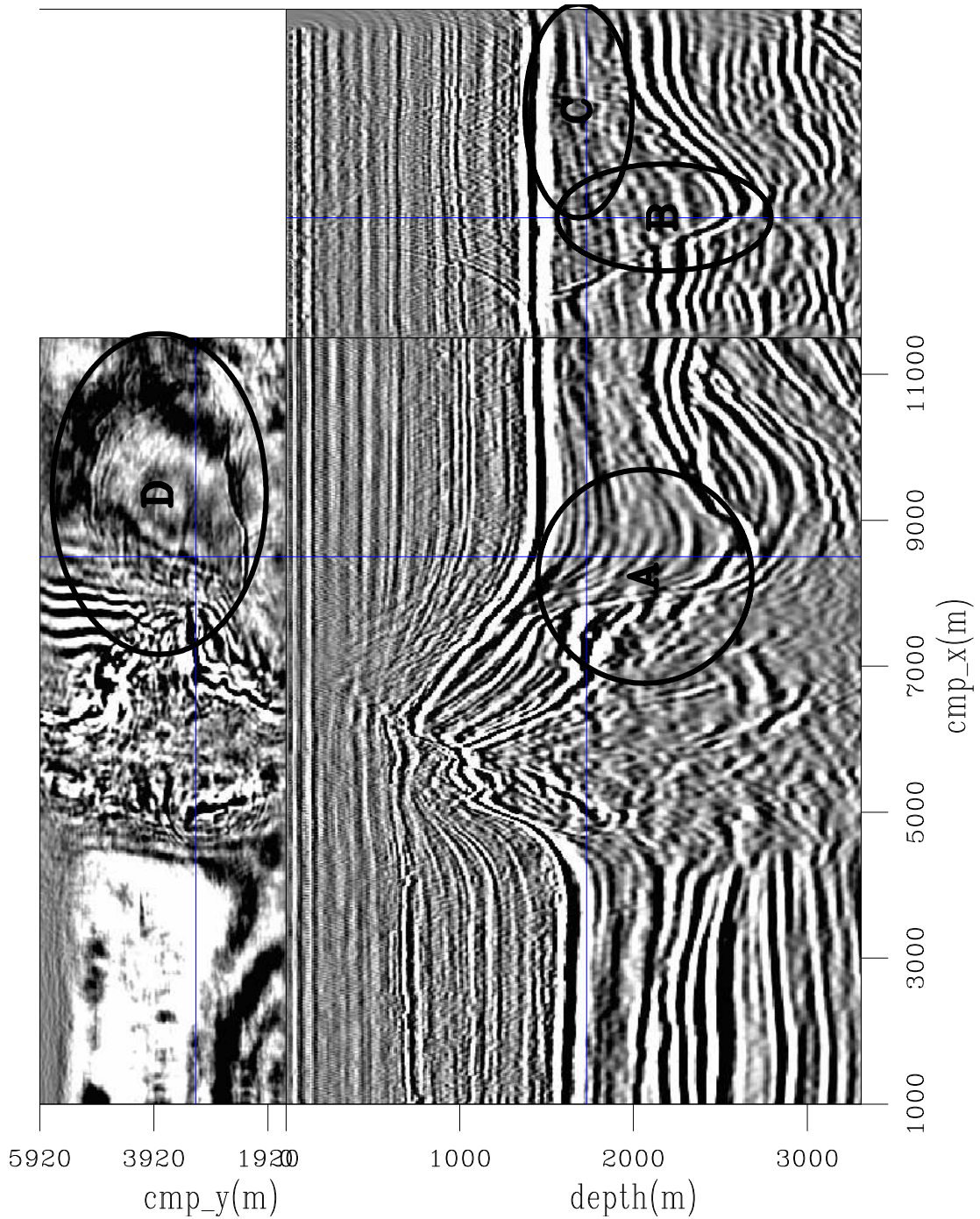


Figure 5.21: Slices through the CAM image with the optimized velocity model of Figure 5.20. Notice the imaging of a big fault close to the salt flank (A), and the focusing of a complex fault system (B, C, and D). 3dex/. 3dex218

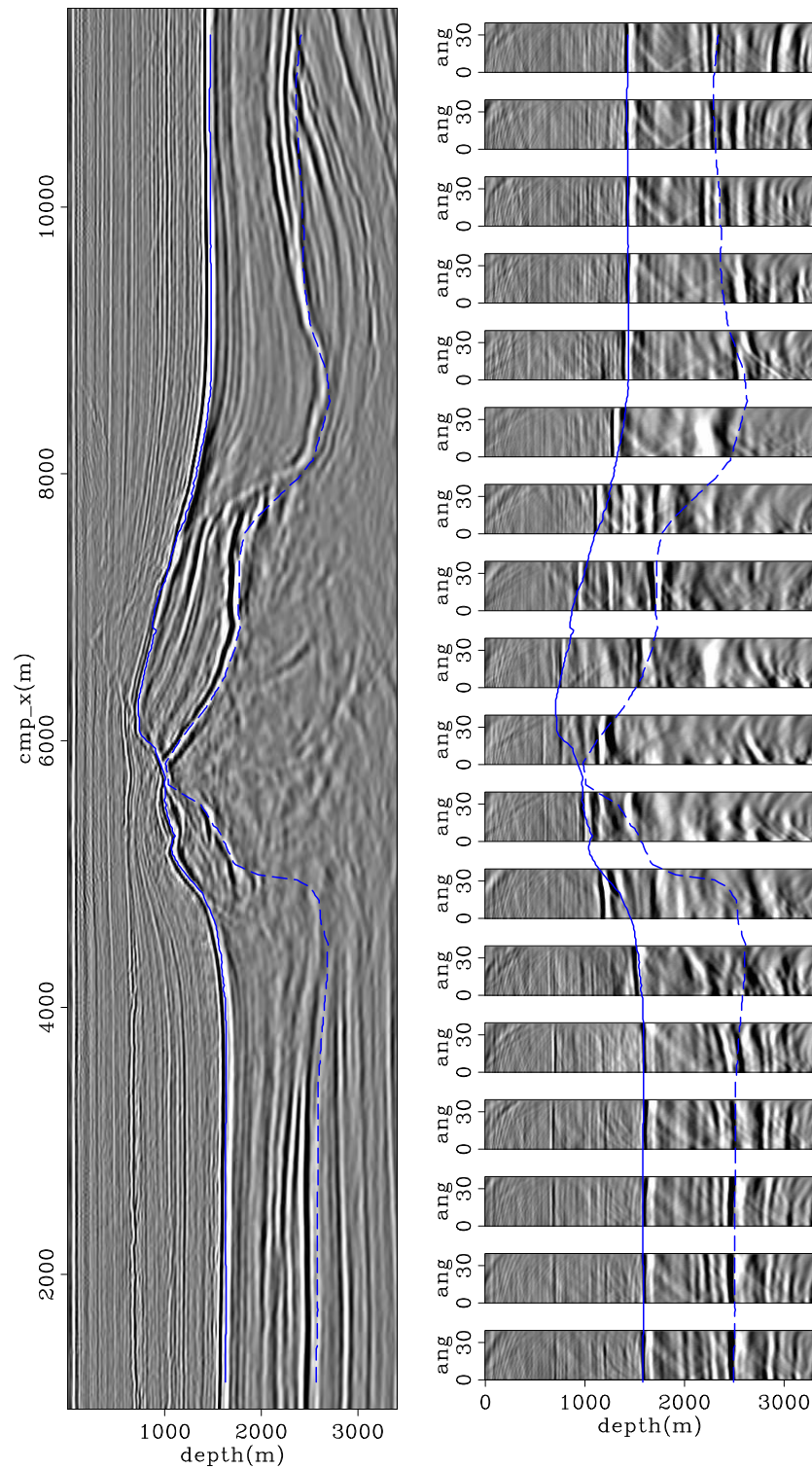


Figure 5.22: In-line 3180 of the CAM image with the optimized velocity model of Figure 5.20. On the left is the zero-subsurface offset section, and on the right ADCIGs. Notice flatter reflectors in the ADCIGs compared to those in Figure 5.10. The continuous blue line is the top of chalk, and the dashed blue line it the base of chalk.

3dex/. 3dex2193180

the top of salt is a source of uncertainty for defining the velocity model below, since it is difficult to manually interpret all the high-wavenumber components of the irregular top of salt. A solution to this problem should use automatic procedures to identify the top of salt (Lomask, 2006; Halpert, 2010).

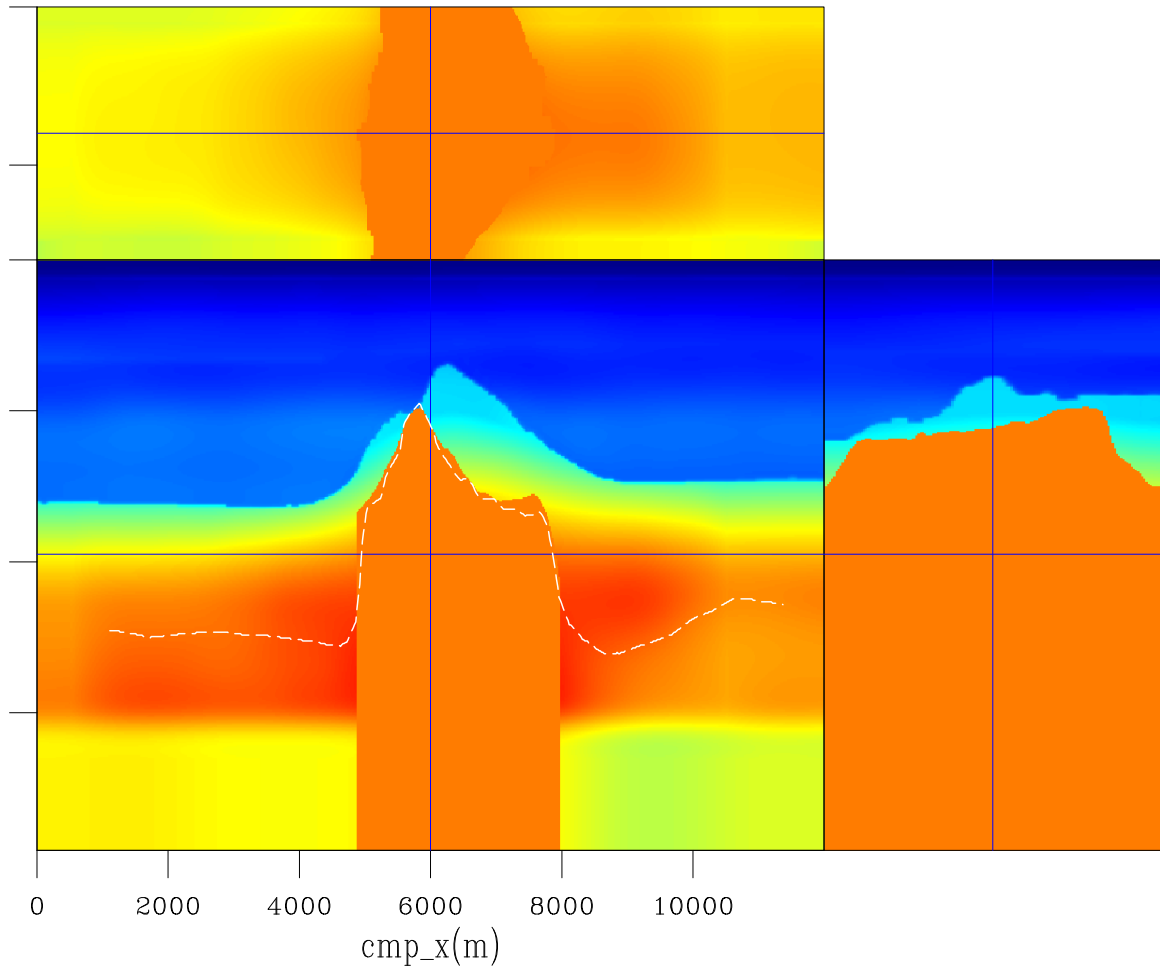


Figure 5.23: Slices through the velocity volume after salt flooding. The dashed white line approximately represents the base of chalk. 3dex/. 3dex311

The CAM migrated image (Figure 5.24) computed with the velocity of Figure 5.23 was sufficiently focused to support the interpretation of the base of the salt. As can be seen in Figure 5.24, the lack of a continuous reflector makes the interpretation of the base of salt challenging. Insufficient illumination due to the limited azimuthal

coverage and irregular shape of the salt body caused the base of salt to be discontinuous. In this situation, prior geological information would be extremely helpful to constrain the interpretation. The lack thereof is another source of uncertainty for defining the velocity model below the salt.

After the base of salt was interpreted, the velocity was edited again (Figure 5.25), so that the salt velocity was confined within the salt body and the initial velocity was inserted below the salt and the chalk layer. With this new velocity model, another run of CAM generated the image in Figure 5.26 from which deeper reflectors are used to model new ISPEWs to be used in ISWET for deeper layers.

SOLVING FOR SUB-SALT VELOCITIES

On the prestack image of Figure 5.27, resulting from CAM with the sufficiently accurate velocity model for the chalk layer and the salt body, seven reflectors were interpreted (Figure 5.28) to be used as the initial conditions for the modeling of 3D ISPEWs for defining sub-salt velocities. Again, 30 pairs of 3D-source and -receiver ISPEWs were generated. These wavefields were collected at a depth of 1650 m, which is the minimum depth used in the velocity optimization. The prestack image used as the initial conditions for the modeling has 33 in-line subsurface offsets with 30 m intervals and a maximum offset 480 m. The CMP interval in the x and y directions is 30 m.

The initial velocity used in the sub-salt velocity optimization is shown in Figure 5.25. The shallower limit for velocity updating is represented by the base of chalk and base of salt, and the deeper limit is 4800 m. The interval between B-spline nodes is 1050 m in the x and y directions and 150 m in the z direction. A maximum of 5% local velocity variation is allowed between iterations, and two function evaluations are performed in the line search.

The evolution of the objective function normalized by its initial value is shown in Figure 5.29. Velocity optimization stopped after 7 iterations because the update of the objective function was smaller than 0.1%. The final objective function dropped

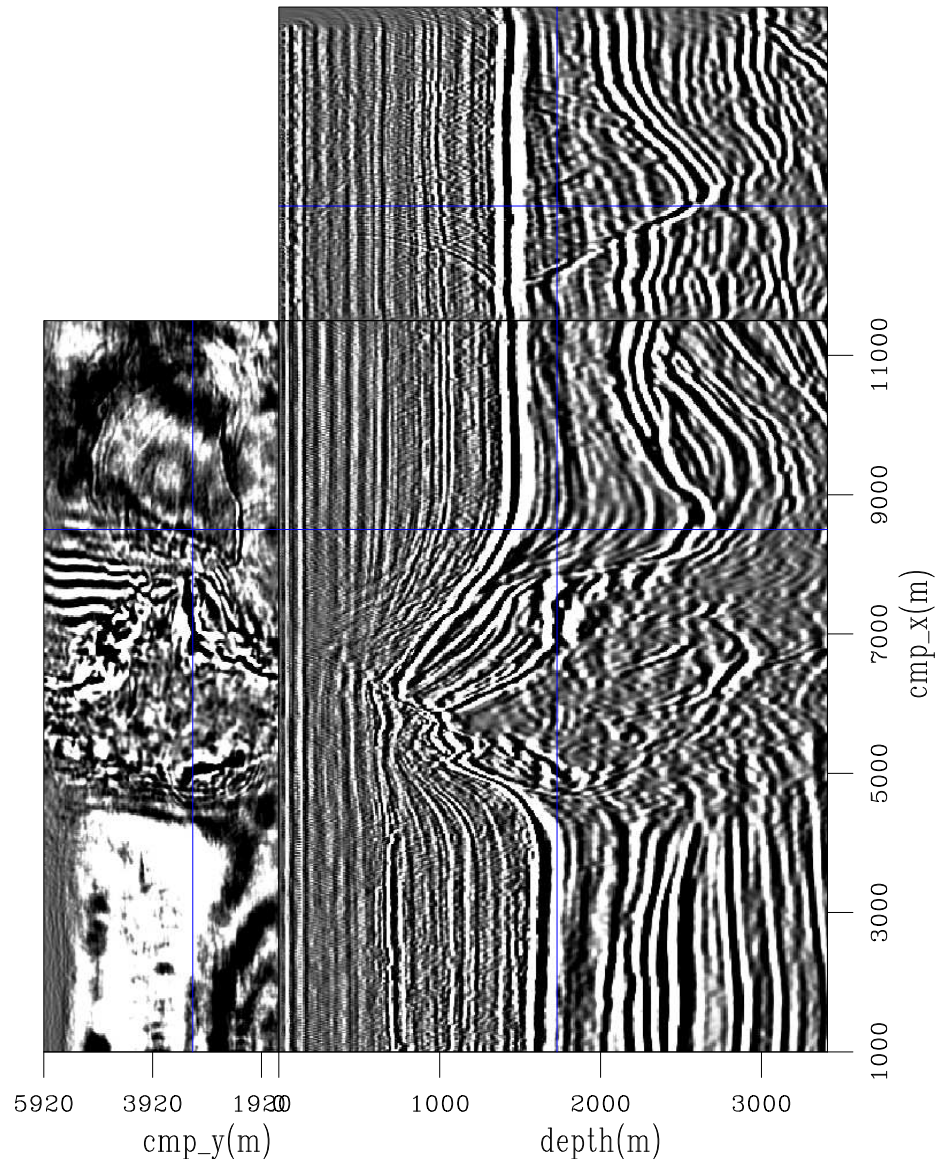


Figure 5.24: Slices through the CAM migrated image computed with the salt flooding velocity model of Figure 5.23. `3dex/. 3dex312`

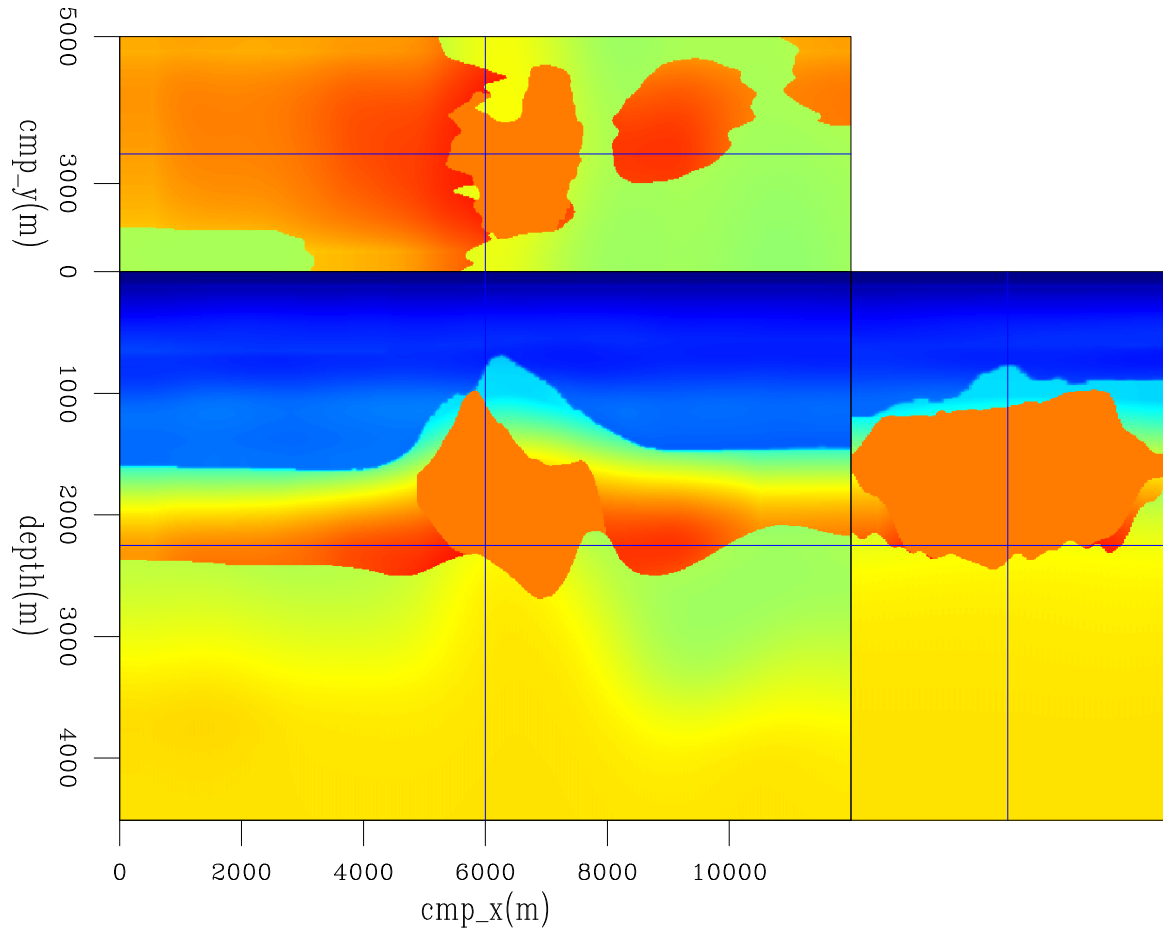


Figure 5.25: Slices through the velocity volume after interpretation of the base of salt. `3dex/. 3dex313`

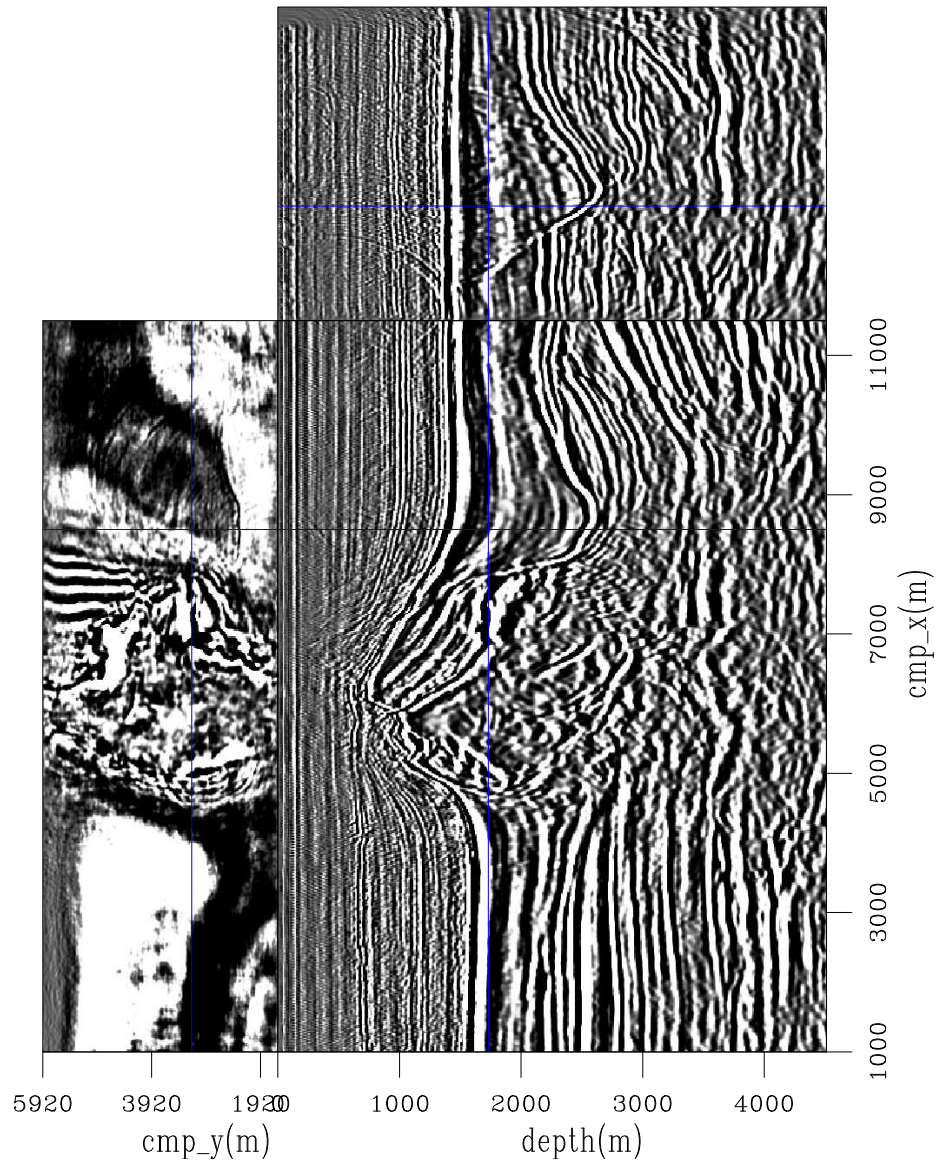


Figure 5.26: Slices through the CAM migrated image computed with the velocity model of Figure 5.25. `3dex/. 3dex314`

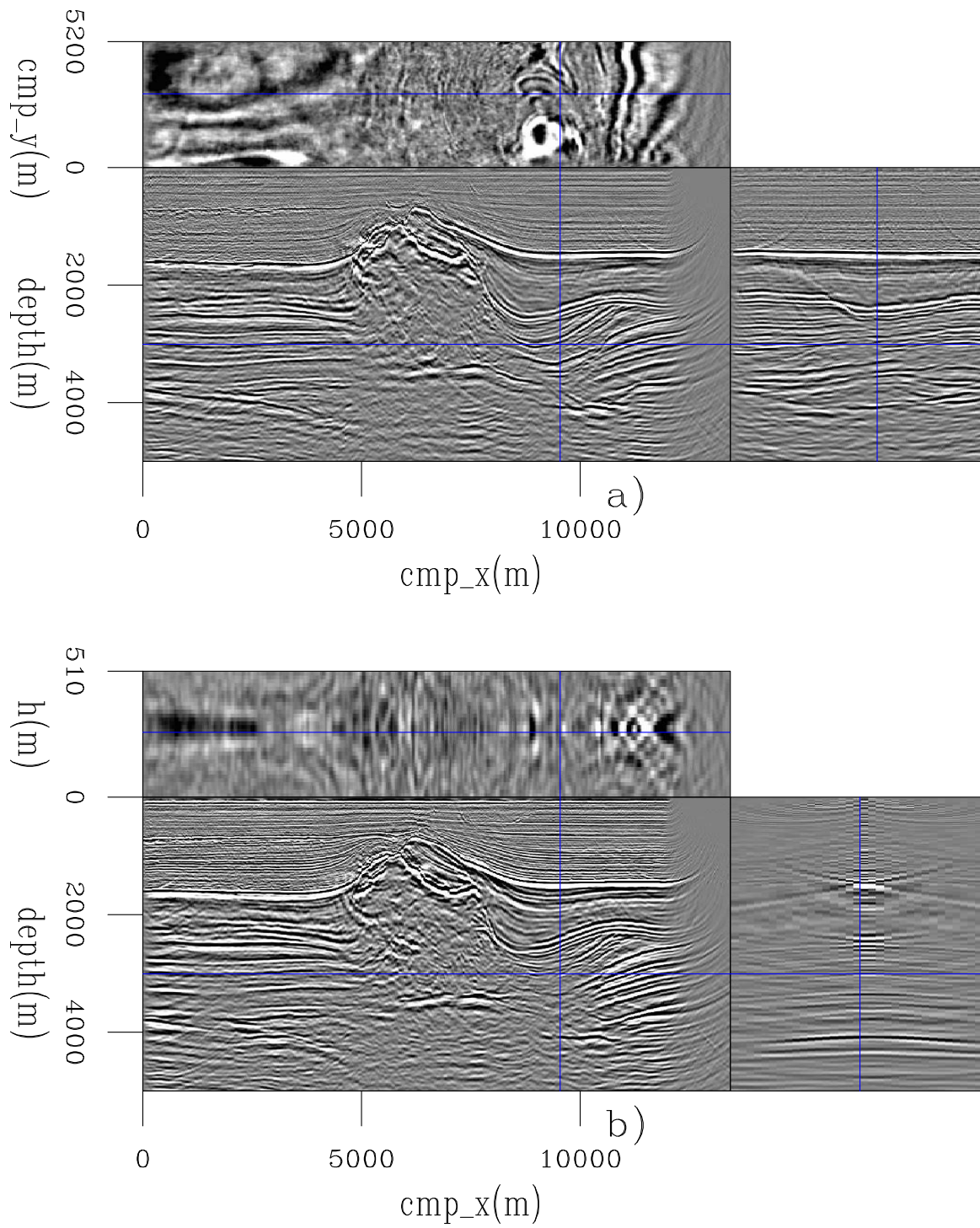


Figure 5.27: Slices through the prestack image computed with the migration velocity of Figure 5.25: a) the zero subsurface offset, and b) the in-line 3520. 3dex/. 3dex400

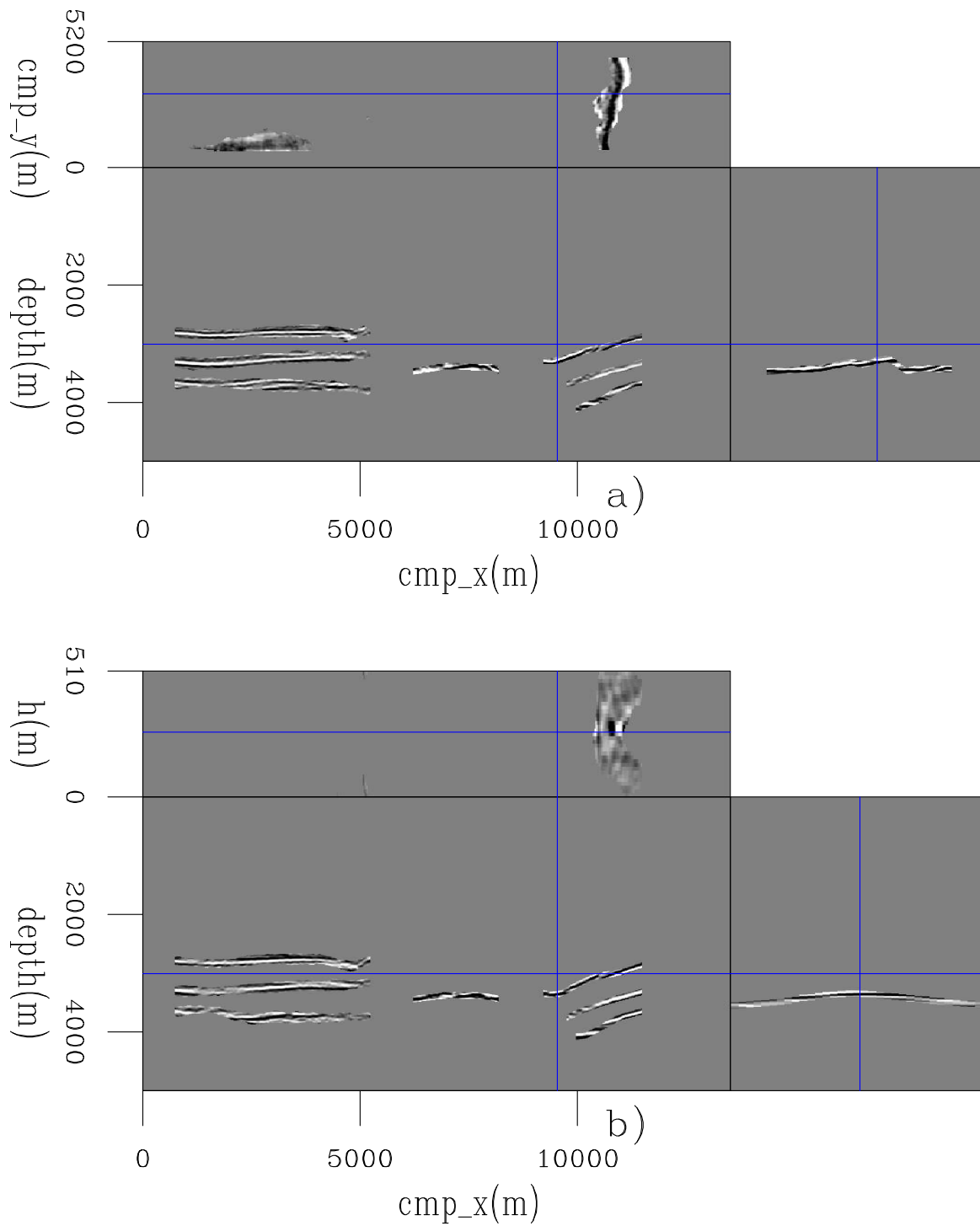
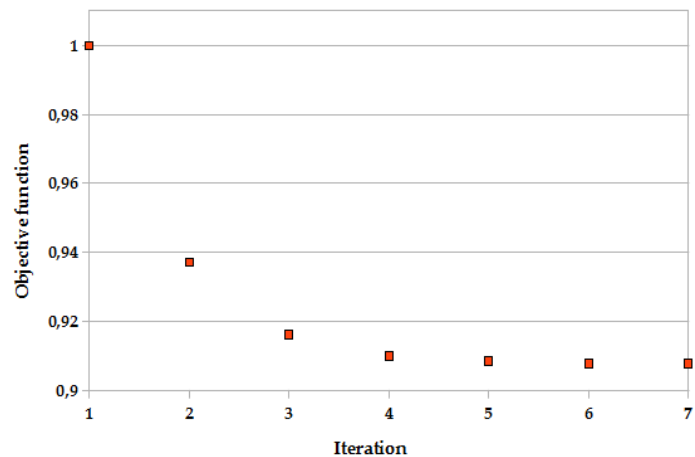


Figure 5.28: Slices through the windowed prestack image, showing the selected reflectors for the modeling of 30 3D ISPEWs to be used in the sub-salt velocity optimization: a) the zero subsurface offset, and b) the in-line 3520. 3dex/. 3dex401

10%. This decrease is small compared to the 40% decrease of the objective function for the velocity optimization of the base of chalk. For the chalk case, only crosstalk from different SODCIGs was generated because only one reflector was used to generate the 3D ISPEWs. For the sub-salt case, in addition to the crosstalk from different SODCIGs, reflector crosstalk was generated since seven reflectors were used as the initial conditions. Hence, the amount of background dispersed crosstalk is greater in the sub-salt case than in the chalk case, explaining the smaller decrease of the objective function in the sub-salt velocity optimization. This is clearly seen when comparing the image for the last iteration of the base of chalk velocity optimization (Figure 5.18) and the image for the last iteration of the sub-salt and sub-chalk velocity optimization (Figure 5.30). The evolution of the velocity model through iterations is shown in Figure 5.31.

Figure 5.29: Evolution of the DVSA objective function of the sub-salt velocity optimization.

3dex/. 3dex402



CAM with the optimized velocity model can be seen in Figure 5.32. For comparison, CAM with the initial velocity model and CAM with the original velocity model are shown in Figures 5.33 and 5.34. When compared with the results using the initial velocity model, the improvements obtained with the optimized velocity model are clear: flatter angle gathers, better focusing of the reflectors, and imaging of the faults. The improvements compared to the original (unmodified) velocity model are also clear: better focusing of reflectors and slightly flatter angle gathers below the salt as well as close to its flanks.

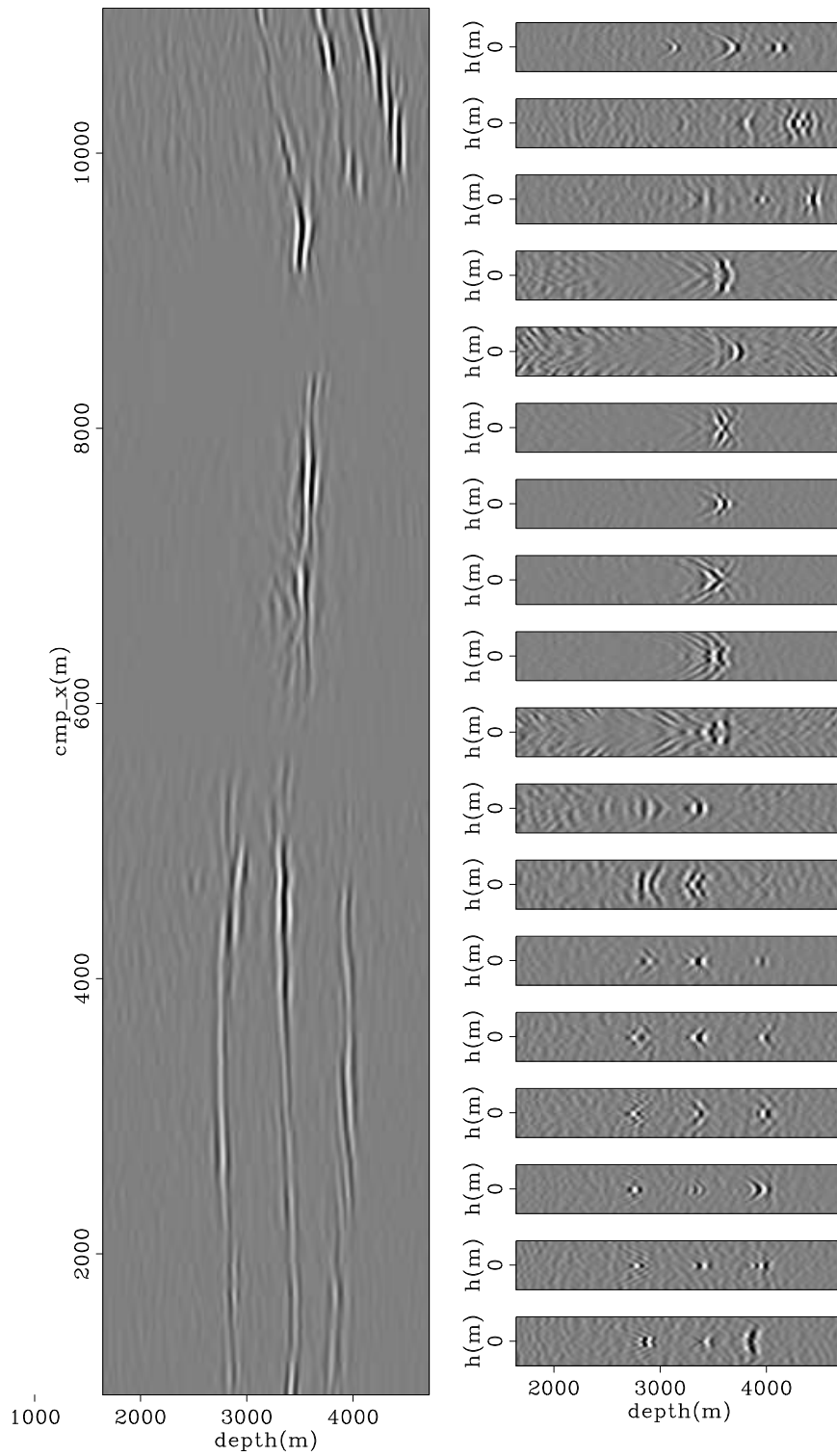


Figure 5.30: In-line 3520 of the image of the last iteration of the sub-salt and sub-chalk velocity optimization. Notice the greater amount of dispersed crosstalk in this image than that of the Figure 5.18. 3dex/. 3dex4000

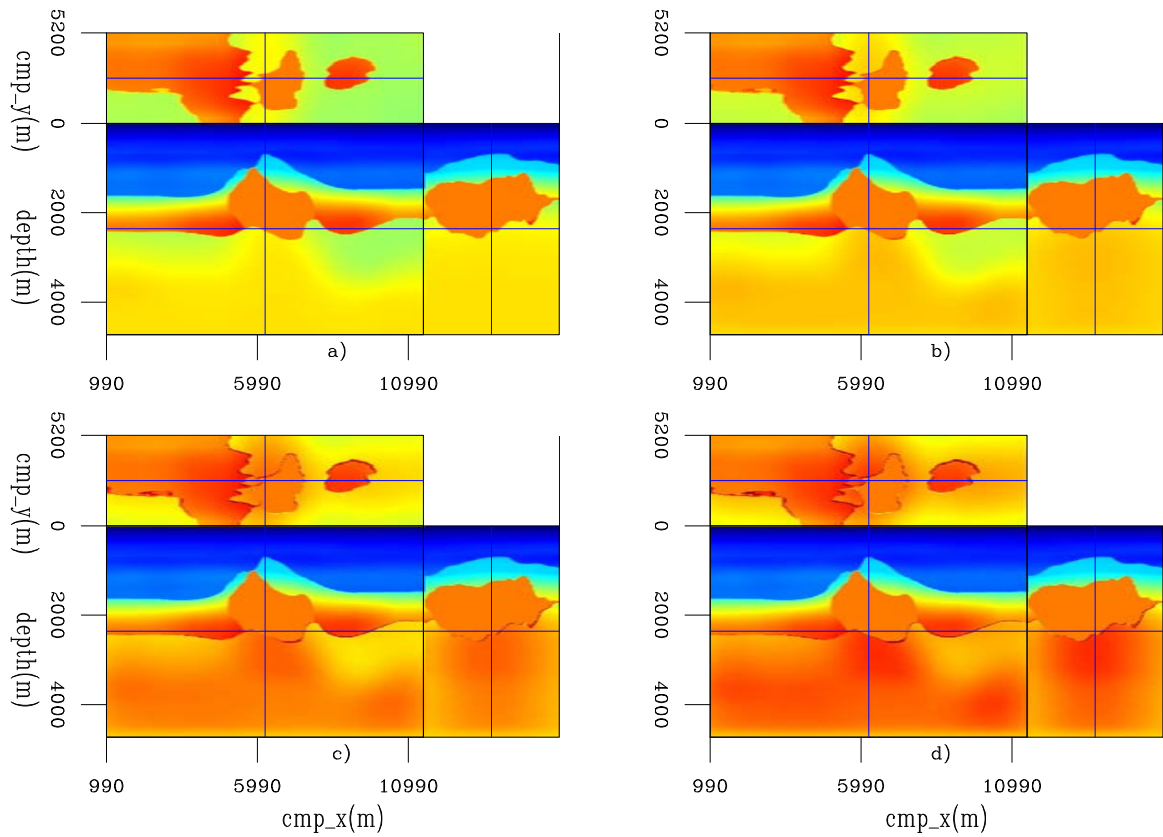


Figure 5.31: Slices through velocity models for: a) first iteration, b) third iteration, c) fifth iteration, and d) seventh iteration. 3dex/. 3dex403

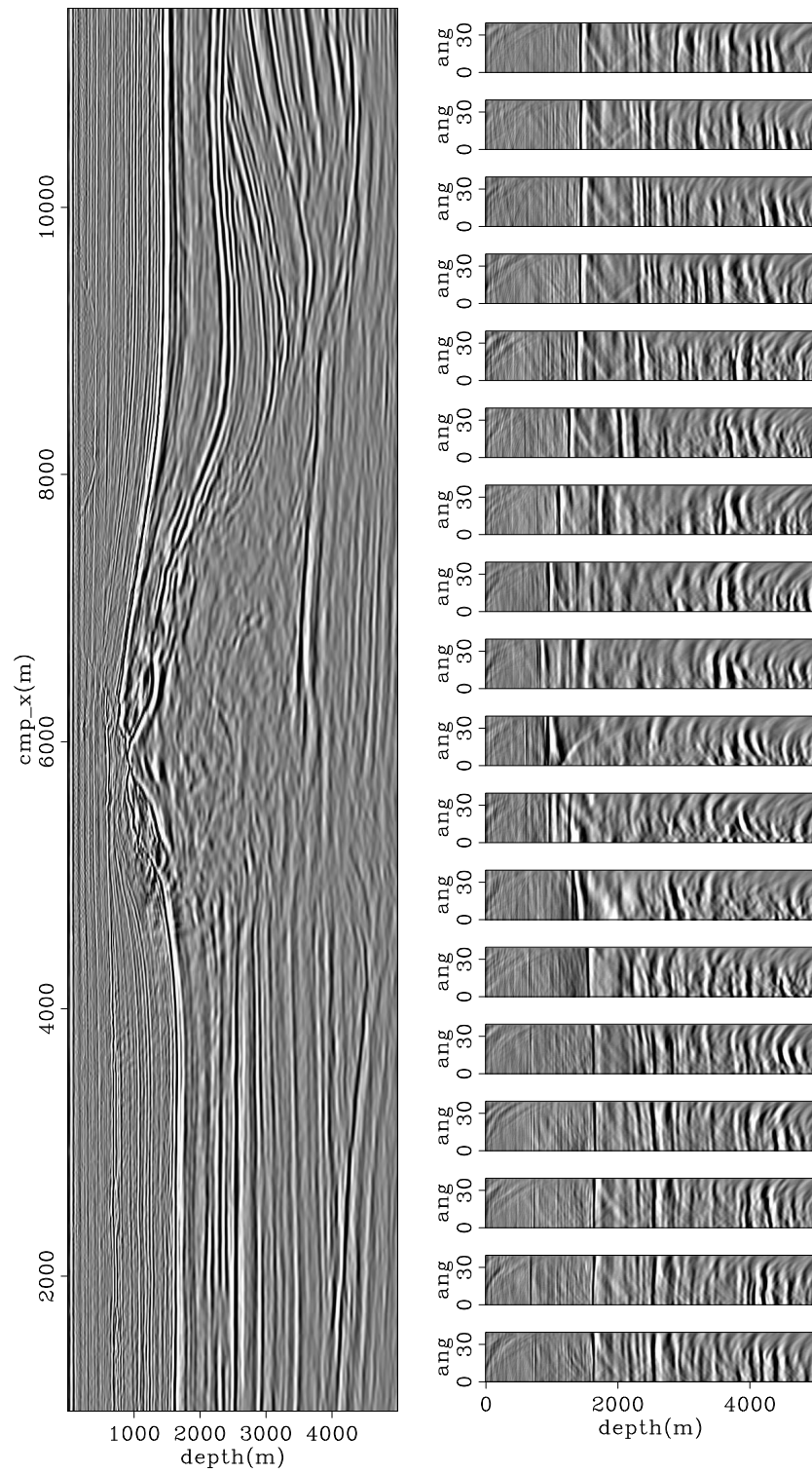


Figure 5.32: In-line 4060 of the CAM image with the final velocity model after optimization for the chalk layer, salt flooding, and sub-salt velocity optimization. On the top is the zero-subsurface offset section, and at the bottom ADCIGs.

3dex/. 3dex404a4060

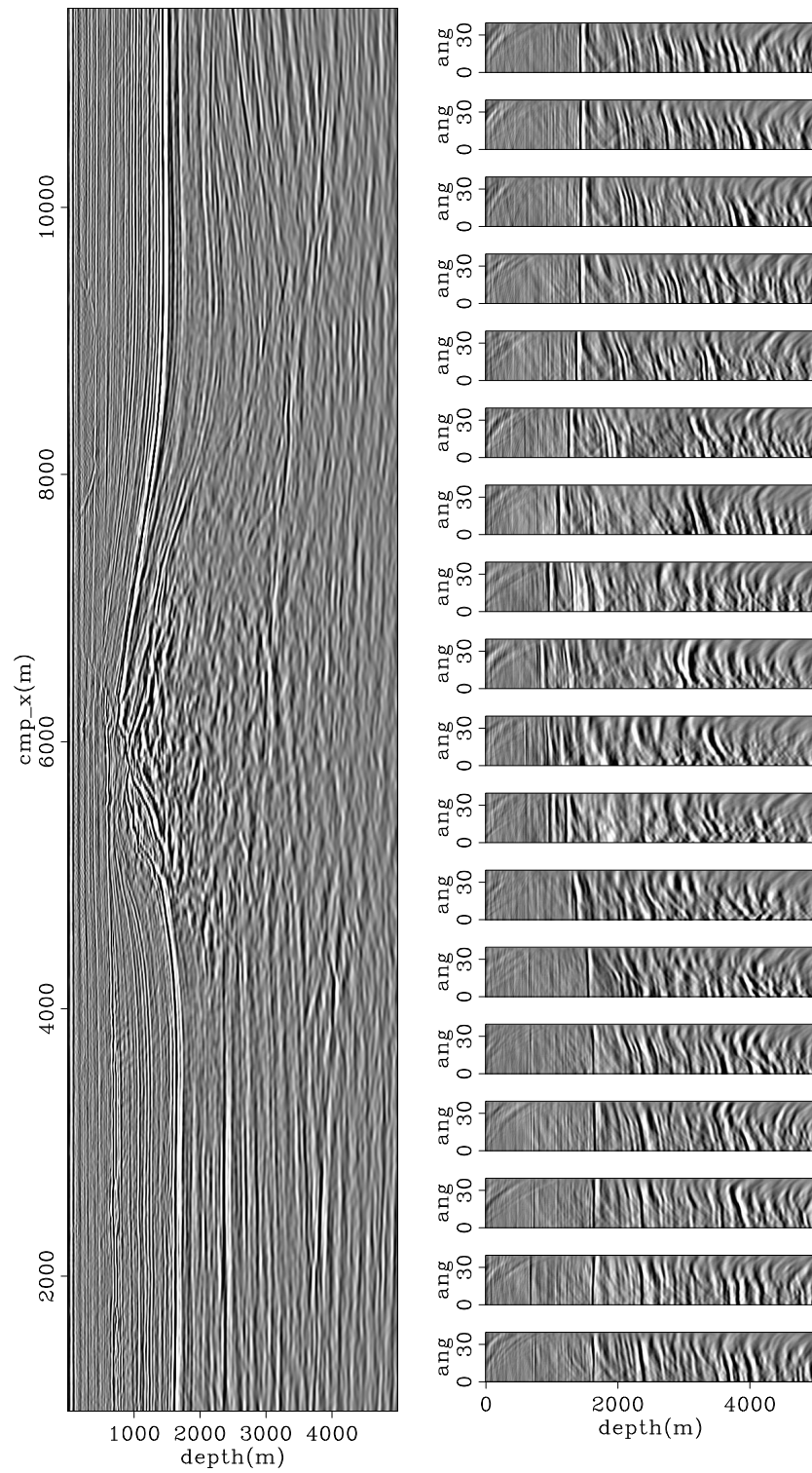


Figure 5.33: In-line 4060 of the CAM image with the initial velocity model. On the top is the zero-subsurface offset section, and at the bottom ADCIGs.

3dex/. 3dex405a4060

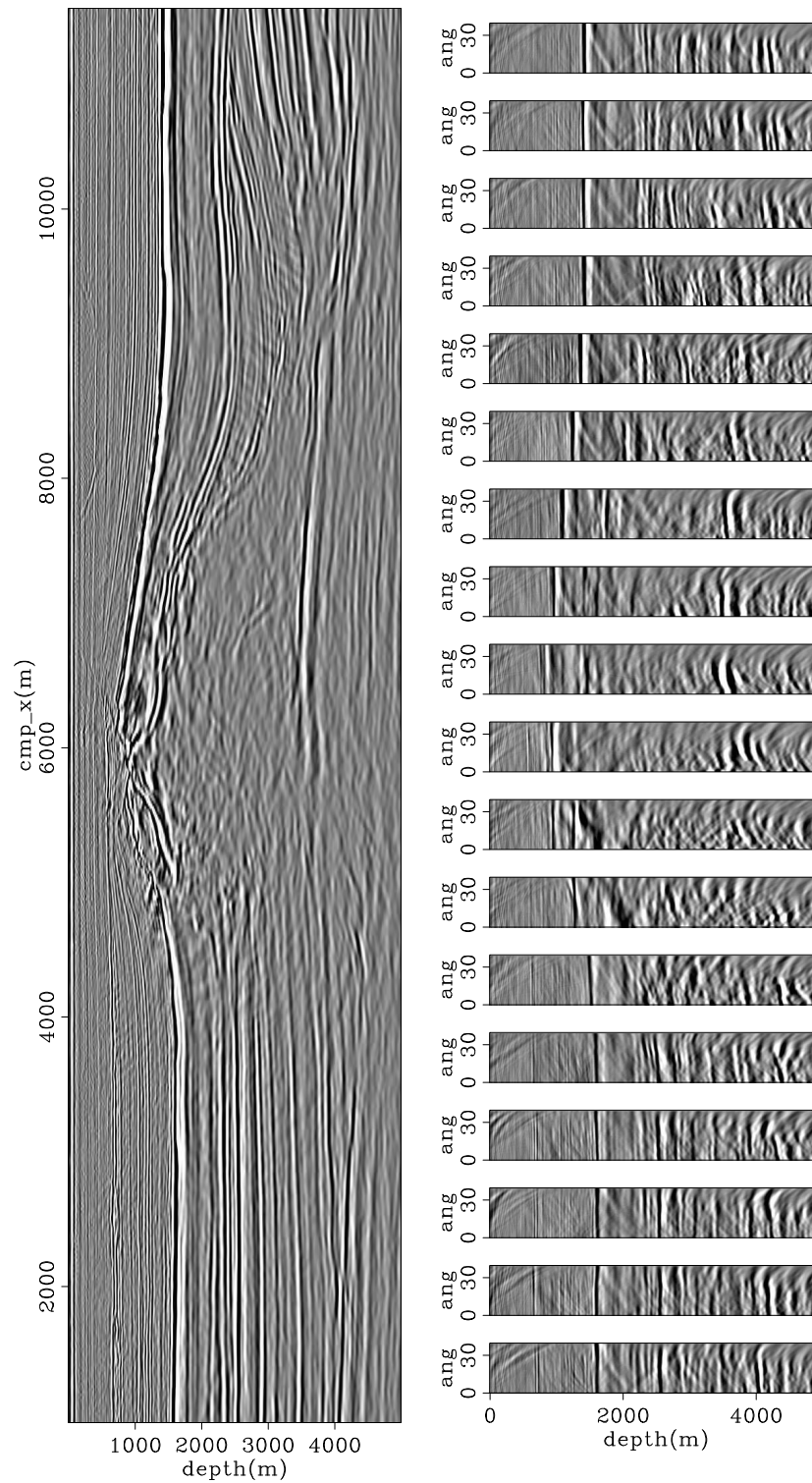


Figure 5.34: In-line 4060 of the CAM image with the original velocity model. On the top is the zero-subsurface offset section, and at the bottom ADCIGs.

3dex/. 3dex406a4060

Next, I show more systematic comparisons of the results computed with the initial, original and the final velocity models.

COMPARISONS

Here, in Figures 5.35, 5.36, and 5.37, I show comparisons for three different sets of in-lines and cross-lines between the CAM images computed with the final velocity model with that computed with the starting velocity model for the sub-salt velocity optimization of Figure 5.25. Using the same sets of in-lines and cross-lines, I also compare the CAM images obtained with the initial, with the original, and with the final velocity models, in Figures 5.38, 5.39, and 5.40. The images are displayed as vertical slices through the migrated cube and show the zero subsurface offset. The left panel of each figure shows the in-line, and the right panel shows the cross-line.

Figures 5.35, 5.36, and 5.37 illustrate the effectiveness of the sub-salt and sub-chalk velocity optimization by comparing CAM images computed with the final velocity model with that obtained using the starting model of Figure 5.25. The improvements in image quality are dramatic, as highlighted by the ovals. Better focusing of sub-salt and sub-chalk reflectors, better fault imaging, and flatter and more unstructured reflectors below the salt body reveal greater accuracy of the final velocity model compared to the starting velocity model of Figure 5.25.

Overall, the final images present better quality than do the initial and original images. Certainly, the final image would help the interpretation and understanding of geological and structural history, adding more value to seismic information in an exploratory study. From Figures 5.38 to 5.40 it is clear the superior quality of the image computed with the final velocity model. This is expressed, for instance, by the good focusing of the base of chalk and reflectors close to the salt flank (Figures 5.39c and 5.40c), the clear delineation of the salt overhang (Figure 5.38c), the flat sub-salt reflectors (Figures 5.38c and 5.39c), and the well defined fault geometry in Figure 5.40c.

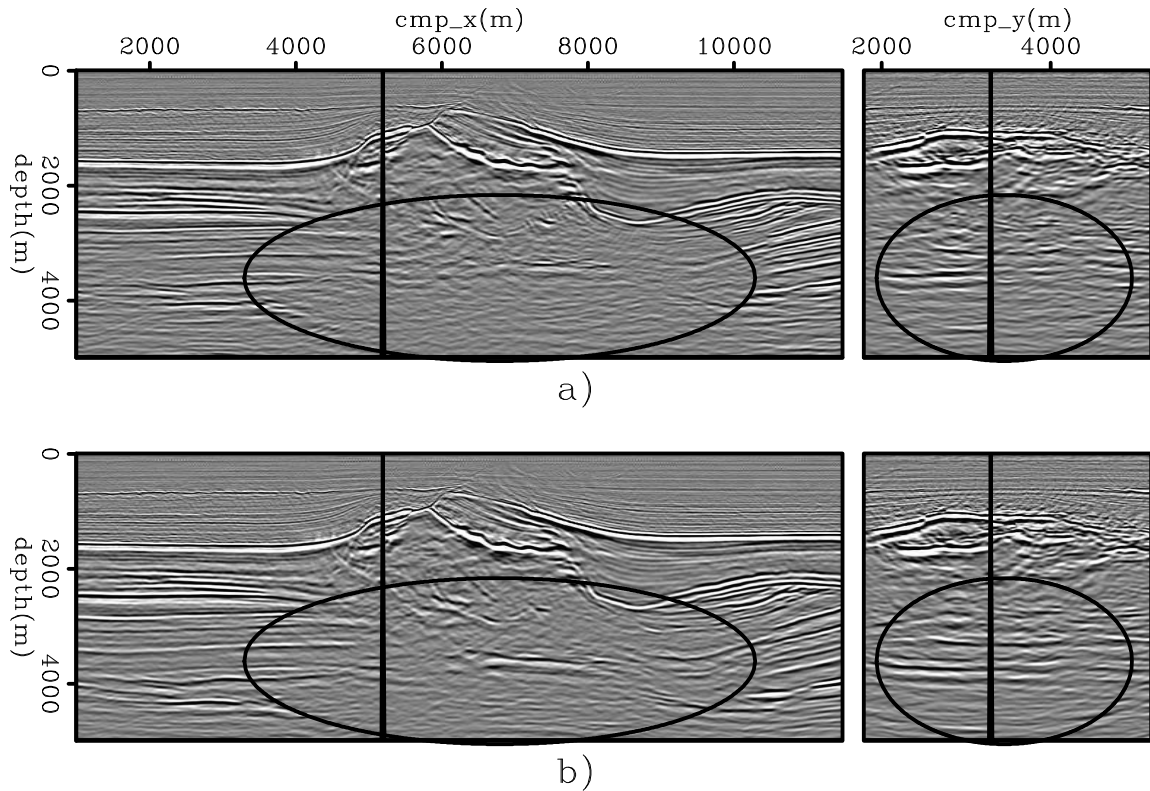


Figure 5.35: On the left panel is the in-line 3320 and on the right panel is the cross-line 5220 of the CAM images obtained with: a) the starting velocity model for the sub-salt and sub-chalk velocity optimization and b) the final velocity model. The oval in the in-line of b) shows better focusing for the sub-salt reflectors as well as for reflectors close to the right salt flank. In addition, to the left of the in-line, unfocused reflectors are revealed after migrating with the final velocity. In the cross-line, the final image shows flatter and more unstructured sub-salt reflectors than in a). 3dex/. 3dex503

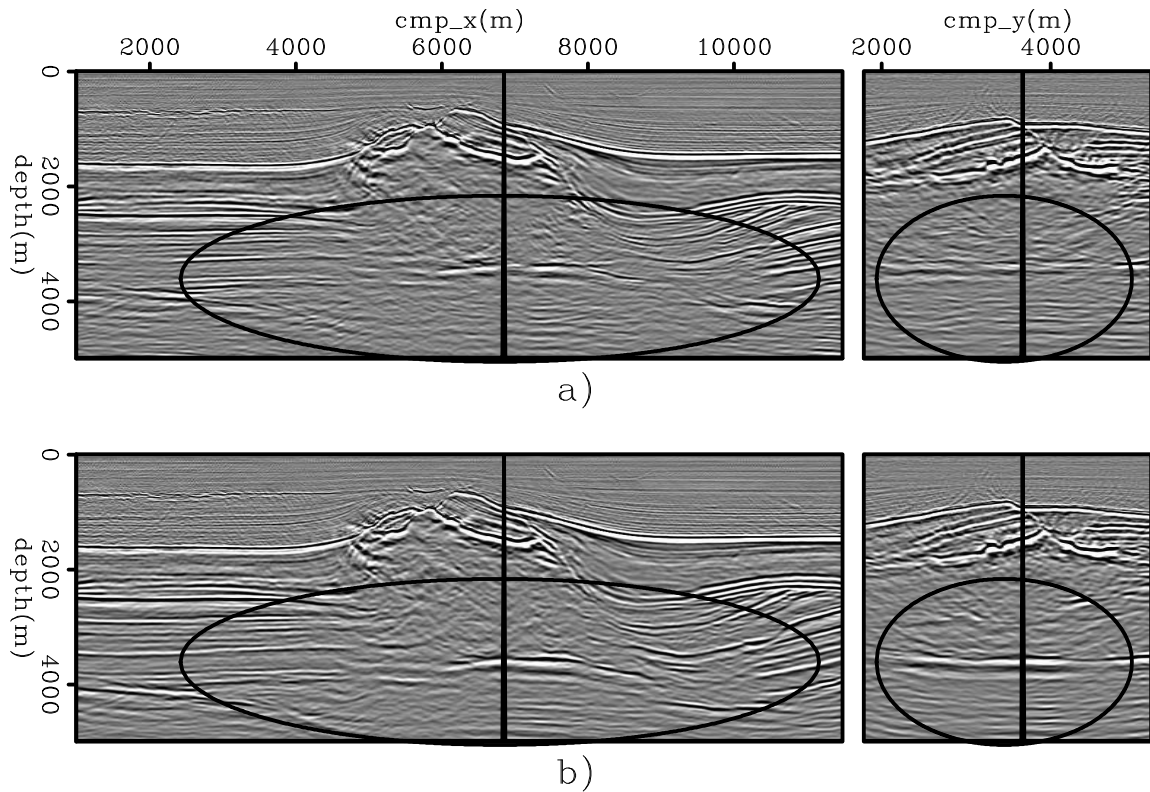


Figure 5.36: On the left panel is the in-line 3680 and on the right panel is the cross-line 6880 of the CAM images obtained with: a) the starting velocity model for the sub-salt and sub-chalk velocity optimization and b) the final velocity model. The oval in the in-line of the final image shows better focusing and continuity for the sub-salt and sub-chalk reflectors and better fault imaging. In the cross-line, the oval in a) shows unstructured deeper reflectors, indicating a sufficiently accurate velocity solution for the layers above. In b), these reflectors remain unstructured, but notice stronger and more focused amplitudes, indicating better velocity solution. 3dex/. 3dex504

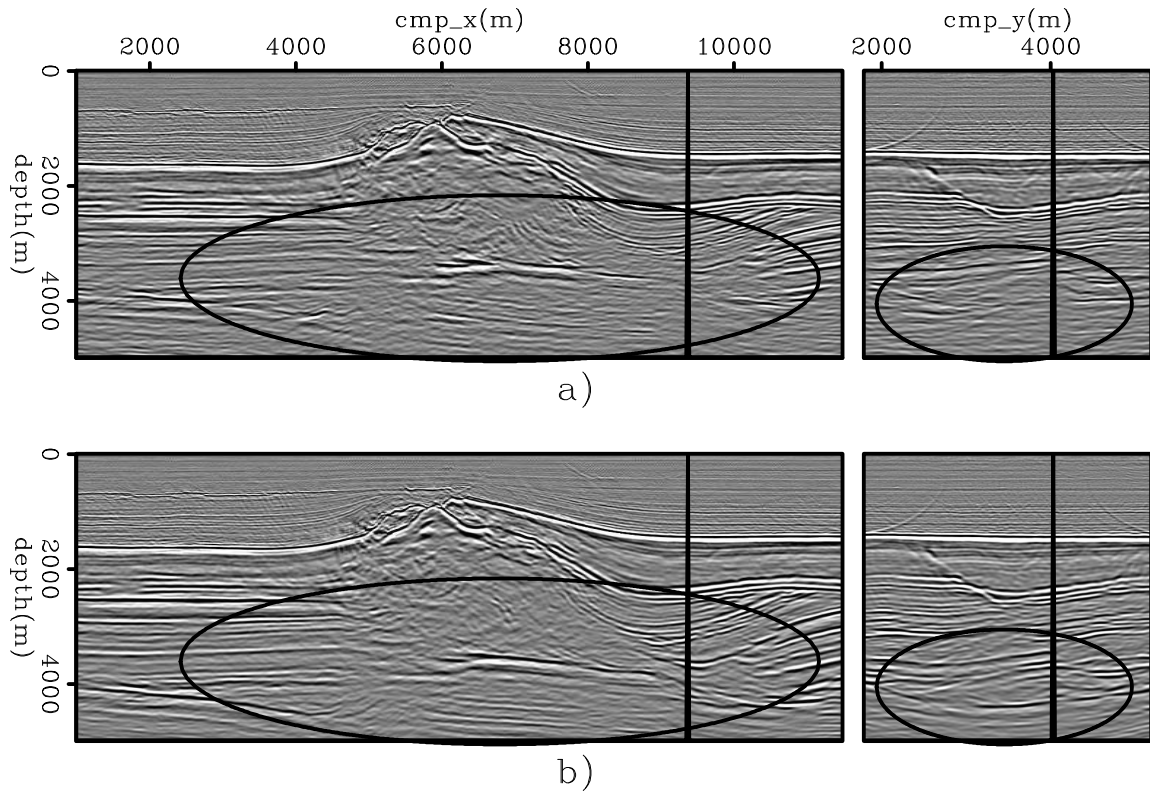


Figure 5.37: On the left panel is the in-line 4060 and on the right panel is the cross-line 9400 of the CAM images obtained with: a) the starting velocity model for the sub-salt and sub-chalk velocity optimization and b) the final velocity model. The oval in the in-line of the final image shows better focusing and continuity for the sub-salt reflectors. In the cross-line, the oval highlights better continuity of the reflectors and better fault imaging not clear in the starting image. 3dex/. 3dex505

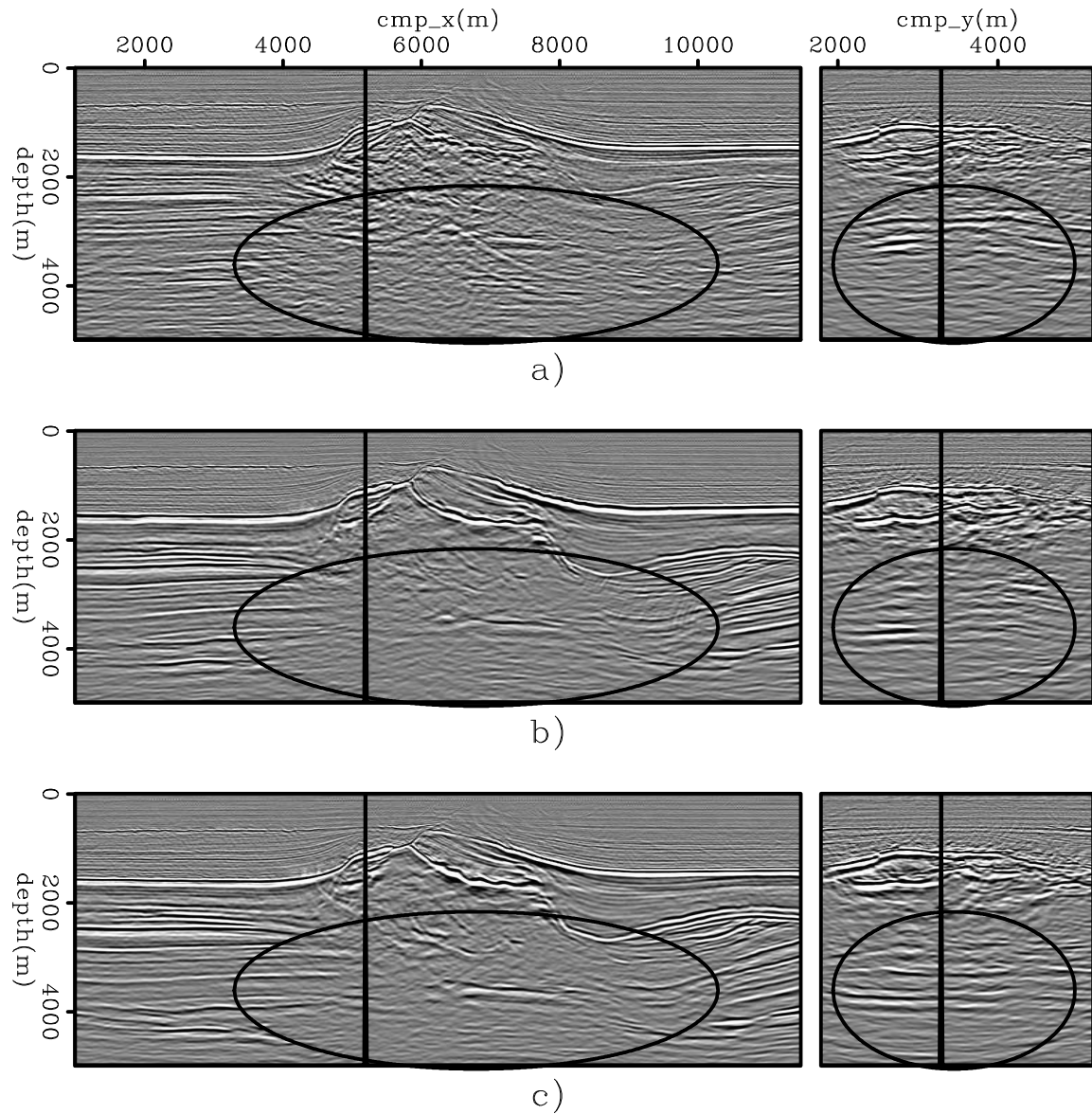


Figure 5.38: On the left panel is the in-line 3320 and on the right panel is the cross-line 5220 of the CAM images obtained with: a) the initial velocity model, b) the original velocity model, and c) the final velocity model after optimization for the chalk layer, salt flooding, and sub-salt velocity optimization. The oval in the in-line of the final image shows better focusing and continuity for the sub-salt reflectors and better delineation of the salt overhang. Besides focusing and continuity, the oval in the cross-line of the final image shows remarkably less structured sub-salt reflectors.

3dex/. 3dex500

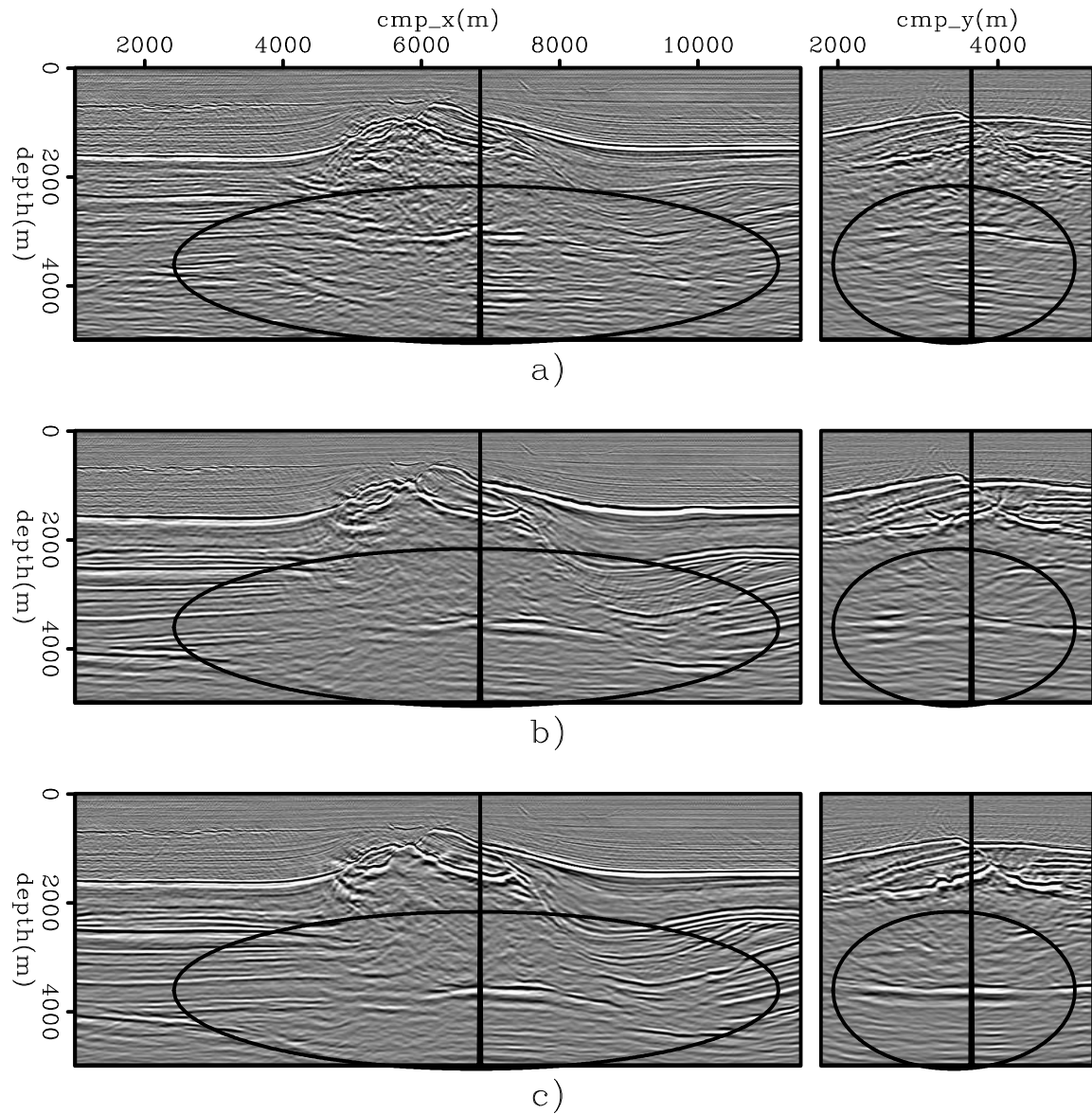


Figure 5.39: On the left panel is the in-line 3680 and on the right panel is the cross-line 6880 of the CAM images obtained with: a) the initial velocity model, b) the original velocity model, and c) the final velocity model after optimization for the chalk layer, salt flooding, and sub-salt velocity optimization. The oval in the in-line of the final image shows better focusing and continuity for the sub-salt reflectors. When comparing b) and c), besides better focusing and continuity, the cross-line in c) shows unstructured sub-salt reflectors not pulled up by velocity errors evidenced by migration swings clearly seen in b). 3dex/. 3dex501

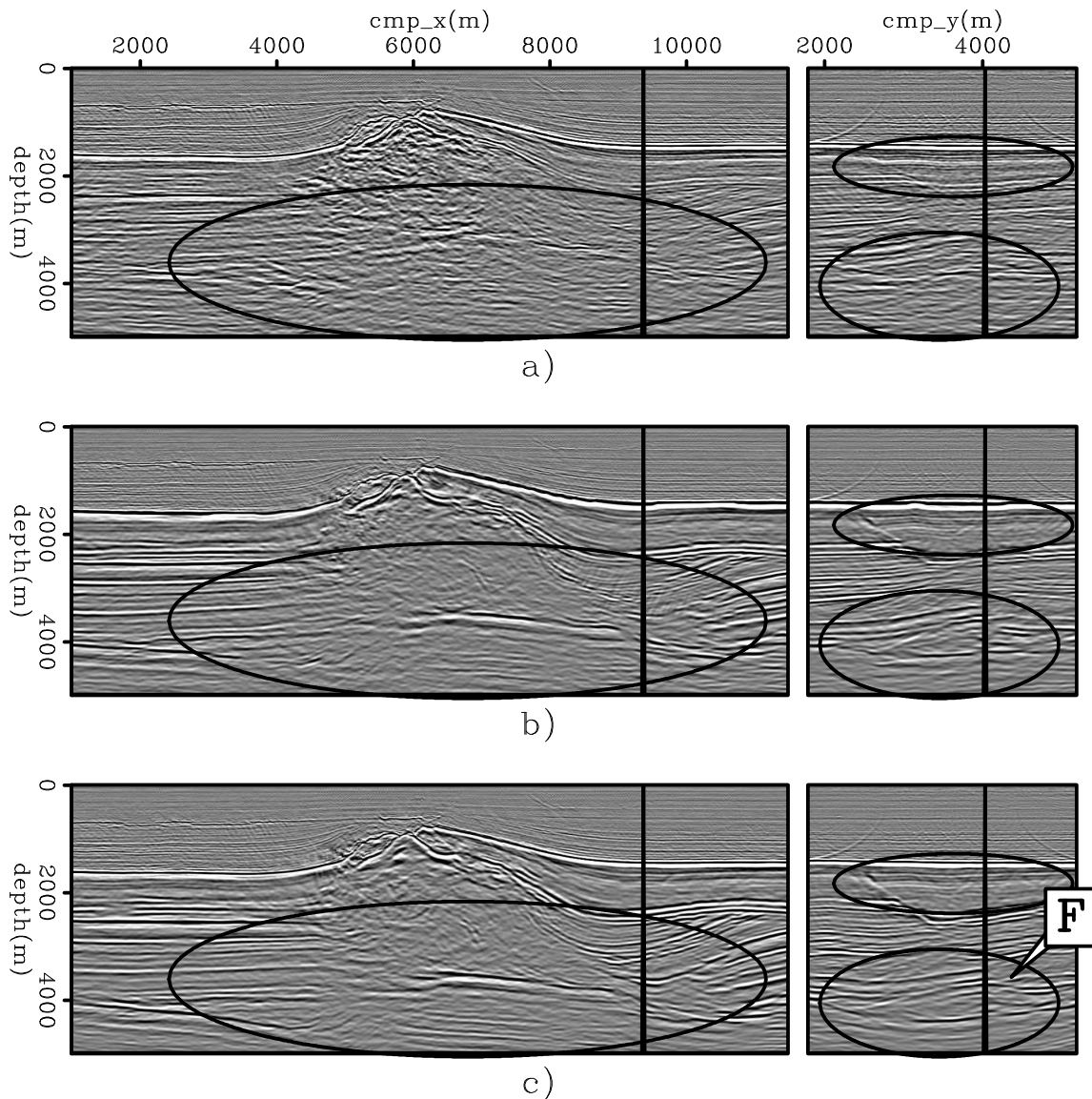


Figure 5.40: On the left panel is the in-line 4060 and on the right panel is the cross-line 9400 of the CAM images obtained with: a) the initial velocity model, b) the original velocity model, and c) the final velocity model after optimization for the chalk layer, salt flooding, and sub-salt velocity optimization. The oval in the in-line of the final image shows better focusing and continuity for the sub-salt reflectors. It is remarkable the better continuity of the reflectors intersected by the vertical line in c) than in b), indicating a much better solution for the velocity model. In the cross-line, the upper oval of the final image shows better definition of subtle faults in the chalk layer, the lower oval highlights better continuity of the reflectors, and the arrow labeled "F" indicates better fault imaging not clear in the initial and original images. 3dex/. 3dex502

CONCLUSIONS

The 3D-field data North Sea turned out to be a very challenging dataset. The challenges were represented by the narrow azimuth configuration and irregular fold of coverage, causing incomplete and irregular illumination of the reflectors. Furthermore, the irregular salt body and intense faulting were difficult targets to delineate and image. The problems with the illumination, evidenced by amplitude irregularity of the gradient of the objective function, were mitigated by properly scaling the prestack image used to model the 3D ISPEWs and the gradient of the objective function, and by smoothing the gradient of the objective function.

Using 3D ISPEWs has proved to greatly accelerate 3D ISWET, due to the small number of wavefields needed to satisfactorily describe the kinematics of the prestack image and the fact that 3D ISPEWs can be computed in a target-oriented manner. These synthesized wavefields made it possible to solve 3D ISWET in an academic environment with limited computational resources. Considering the computational resources available in the industry, using 3D ISPEWs can turn 3D ISWET into an interactive process, which can yield more reliable solutions.

Solving for migration velocity in a target-oriented manner with wave-equation methods allows updating the velocity model not only within a limited depth range, but also within a limited lateral extent. This is achieved by selecting a specific portion of a reflector or group of reflectors that still present residual moveout. This feature was demonstrated when updating the velocity model in the vicinity of the salt body, using only a small portion of the reflector corresponding to the base of chalk close to the salt.

Besides the computational gain, 3D ISPEWs were able to provide reliable velocity updates, even starting from a velocity model far from being accurate. Using the final velocity model produces a CAM image with quality superior to that obtained with the initial velocity model, as expected. Moreover, the image computed with the final velocity model is more accurate than that computed with the original velocity model, with better focusing and continuity of the sub-salt reflectors and better fault imaging.

ACKNOWLEDGMENTS

I would like to thank Bob Clapp for making available the common-azimuth migration code and for continuously improving SEP's 3D-interpretation and visualization capability. I am indebted to Dennis Michael, manager of the High Productivity Technical Computing (HTPC) initiative hosted by CEES, for his continuous support.